2016•2017
FACULTEIT INDUSTRIËLE INGENIEURSWETENSCHAPPEN
master in de industriële wetenschappen: nucleaire technologie

Masterproef

Feasibility of a 3D printed bolus integrated with polymer gel dosimetry

Promotor :
Prof. dr. Brigitte RENIERS

Promotor :
prof. dr. ir. TOM DEPUYDT

Copromotor :
ir. STEVEN MICHIELS

Matthijs Sevenois

Scriptie ingediend tot het behalen van de graad van master in de industriële wetenschappen: nucleaire technologie

Gezamenlijke opleiding Universiteit Hasselt en KU Leuven

2016•2017

Faculteit Industriële ingenieurswetenschappen

master in de industriële wetenschappen: nucleaire technologie

Masterproef

Feasibility of a 3D printed bolus integrated with polymer gel dosimetry

Promotor :
Prof. dr. Brigitte RENIERS

Promotor :
prof. dr. ir. TOM DEPUYDT

Copromotor :
ir. STEVEN MICHIELS

Matthijs Sevenois

Scriptie ingediend tot het behalen van de graad van master in de industriële wetenschappen: nucleaire technologie

universiteit hasselt | KU LEUVEN

Acknowledgement

I would like to thank the various people who helped me to create this thesis, without their support this could not have been realised.
First, I would like to thank my parents for allowing me to realize my own potential. Special thanks go to ir. Steven Michiels for his ongoing support and advice throughout the year. I am very grateful for the time he spent helping with the technical and practical aspects of my thesis. I would also like to express my gratitude to dr. Kenneth Poels and dr. Ronald Peeters who were always ready to help whenever they could. Additionally I would like to thank Stijn Roden and Hilde Geeraerts for sharing their knowledge and support in the lab. And last but not least prof. dr. Brigitte Reniers and prof. dr. ir. Tom Depuydt for their advice, insights and for giving me the opportunity to work on this interesting project.

Contents

List of Tables

List of Figures

List of abbreviations

QA: Quality assurance
IMRT: Intensity modulated radiation therapy
VMAT: volumetric modulated arc therapy
IVD; in-vivo dosimetry
PT: proton therapy
EBT3: type of radiochromic film
GTV: gross tumour volume
CTV: clinical target volume
PTV: planned target volume
DVH: dose volume histogram
MLC: multi leave collimator
MU: monitoring units
ROI: region of interest
ICRU: international commission on radiation units & measurements
EPID: electronic portal imaging device
a-Si: amorphous silicon
TPS: treatment planning system
SOBP: spread out Bragg peak
RBE: relative biological effectiveness
γ-map analysis (3%/3 mm): The agreement between a measured and predicted radiation dose is expressed by the gamma score for each measurement point hereby allowing a dose difference of 3% or 3 mm distance or any quadratic combination of dose difference and distance [1].
EBRT: external beam radiation therapy
PAGAT: polyacrylamide gelatine gel fabricated under atmospheric conditions
R_2: inverse of the transverse relaxation time (T_2)

Abstract (Dutch)

Intensiteitsgemoduleerde radiotherapie (IMRT) resulteert in een homogeen bestraald target doelvolume terwijl de omringende risico organen optimaal gespaard worden. In deze gevallen is een gedetailleerde in-vivo fluentiemeting wenselijk. Weefsel equivalent materiaal, een bolus, wordt geplaatst op de huid wanneer oppervlakkige tumoren bestraald moeten worden. 3D geprinte bolussen gevuld met polymeergel werden behandeld om aan deze voorgaande voorwaarden te kunnen voldoen. Dit zou de hele fluentie van het stralingsveld kunnen vastleggen in plaats van de huidige punt detectie methode.

2 verschillende runs werden behandeld bestaande uit elk 2 3D geprinte structuren. Elke print had een set van kalibratie tubes die bestraald werden tot nauwkeurig gedefinieerde dosissen. Tijdens de tweede run werden kalibratiecurven van zowel intra- als interscan uitgewisseld. MRI beeldverwerking werd gebruikt om R2 mappen van de gel te verkrijgen die vervolgens geconverteerd werden met behulp van de R2-dosis kalibratiecurve. Gexporteerde dosisvlakken vanuit het TPS (AAA v10) en EBT3 gafchromische films werden vergeleken met de geregistreerde dosis in de gel met behulp van slice selectie en gamma criteria evaluatie (3%/3 mm). Scores in de tweede run gingen van 11.61% tot 97.04% wanneer vergeleken met het TPS en van 44.81% 93.68% met de EBT3 film.

Geldosimetrie gentegreerd in een 3D geprinte bolus is haalbaar en resulteert in een goede overeenkomst met de filmmeting en TPS dosisvoorspellingen wanneer strikte protocollen voor het maken, bestralen en uitlezing van de gel gehanteerd worden. Verder verbeteringen in nauwkeurigheid in dosimetrie kunnen behaald worden met een adequate tubekalibratie en temperatuurs-gecontroleerde MRI uitlezing.

Abstract (English)

Intensity modulated radiotherapy (IMRT) treatments result in an homogeneous irradiation of the target volume while optimally sparing the surrounding organs-at-risk. For patients in-vivo treatment verification of IMRT, a detailed measurement of the delivered fluence is desirable. When the target volume is located superficially, tissue-equivalent bolus is placed on the patients skin. 3D printed boluses filled with a polymer gel are assessed to meet the demands of IMRT treatment verification. This could capture the whole radiation fluence instead of currently applied point detector measurements.

2 runs were assessed each consisting of 2 printed cuboids with each a set of calibration vials which were irradiated to well-defined doses. During the 2nd run calibration curves were switched. This was done using intra-scan and inter-scan images. MRI imaging was used to obtain R2-maps of the gel which were then converted to dose using the R2-dose calibration curve. TPS (AAA v10) calculated dose planes and EBT3 gafchromic film dose measurements were compared to the dose in the gel by slice selection using dose gamma evaluation (3%/3 mm). Agreement scores for the second run ranged from 11.61% up to 97.04% when compared to the TPS and from 44.81% till 93.68% when compared to EBT3 film.

Gel dosimetry for filled 3D printed boluses is feasible and results in good dose agreement with film dose measurements and TPS dose prediction when strict protocols for gel fabrication and MRI read-out are used. Further improvements in dosimetry accuracy of the in-filled gels is expected with an adequate vial calibration and temperature controlled MRI read-out is obtained.

Chapter 1

Context and goals

1.1 Background

Cancer is a disease which becomes more and more frequent as the population ages. Statistics from the WHO in 2008 predicted an increase in new cases from 12.4 million to 20 million worldwide by 2030. Lung cancer is an example which has a great death toll. Other frequent occurring cancers are: prostate, stomach, breast, cervix, uteri and colorectal [2].
Cancer occurs when normal cellular genes that control cell proliferation, survival and invasion/motility (proto-oncogenes) are altered, resulting in an uncontrolled cell growth. Typical characteristics of these cells are uncontrolled cell division, enhanced survival and dissemination [3].

Radiotherapy aims to deliver a lethal dose of radiation to biological abnormal cells while sparing the healthy surrounding tissue [4]. Some of these tumours could be superficial and situated near the surface of the skin, i.e. basocellular skin cancer melanoma. In these cases a bolus is placed onto the skin to ensure a maximal dosage on the region of interest. However in some cases currently available boluses are inconvenient to fit properly around complex curved structures situated in the head and neck region [5].

3D printing is gaining more and more interest for various applications in radiotherapy such as a bolus to be able to irradiate shallow tumours. Additive manufacturing offers a high degree of flexibility in object shaping and nowadays desktop size printers come at entry-level prices with a wide range of materials. These printed boluses should be able to align better with the contours of the patient than the commercially available boluses.

Radiotherapy is always focused on treating tumours as accurately and efficiently as possible. In-vivo dosimetry (IVD) could be useful here. IVD corresponds to the quantification of the delivered dose during treatment [6]. A 3D printed bolus could be combined with a 3D in-vivo dosimetry detector to be able to verify if the delivered dose was applied correctly.
The need for reliable 3D dose distribution verification becomes more pronounced as more and more high conformal complex radiotherapy techniques (IMRT, VMAT, PT) are being introduced in the clinic. Conformal doses are delivered dynamically which means dose rate and/or gantry speed and the MLC shape of the beam will vary continuously. An integrating dosimetry technique could prove to be useful here to capture the fluence of the field.

1.2 Problem

In radiotherapy treatment, the depth dose profile of photons typically deposits a maximal dose a few centimetres deep within the patient. That's why irradiation of shallow tumours on or just beneath the skin require an additional build-up, on top of the skin by means of a bolus. Currently these boluses consist of loose and flexible flaps. Firstly, 3D printing makes the bolus patient specific. It is also known that the shape of neck carcinoma changes a lot during the treatment. Here 3D printing could offer the advantage of making and remaking the bolus patient specific as to enhance the fitting of the bolus to the skin.

As new radiation dose delivery techniques are being introduced, new problems also arise. The implementation of intensity modulated radiation therapy (IMRT) and volumetric modulated arc therapy (VMAT) as high precision conformal techniques require high precision quality assurance (QA)[7]. One of the consequences of these high conformal techniques is the chance of partially missing the target volume due to uncertainties in patient localisation, machine failures, set-up variations and others [8]. These verifications consist mainly of absolute point dose measurements with a small volume dose ionization chamber and 2D fluency verification with an array of detectors or film [7]. Subsequently there is a need for a detector which could measure the fluence in 3D to verify IMRT and VMAT plans.

In-vivo dosimetry would be a favourable technique to evaluate the applied dose distributions during the treatment. This could reduce the number of treatment errors which cannot be detected by routine QA. Radiotherapy should continue to strive to reduce the harm to the patients. IVD is therefore suggested as a final verification of the plan [9]. Mijnheer B. *et al.* wrote in his article that 3D in-vivo dosimetry may be expected during the verification of IMRT, VMAT, proton and ion beams. This technique has been suggested as a pragmatic tool for plan adaptation during treatment [6].

The previous mentioned bolus could be integrated with 3D in-vivo dosimetry technology. However assessment and evaluation of the delivered dose in 3D is still no common asset in a clinical setting. To be useful in a clinical setting 3D IVD would require a read-out after each fraction to adjust the dose of the remaining fractions [10].

1.3 Structure of the thesis

The purpose of this paper is a study to determine the feasibility of implementing a three dimensional printed bolus filled with a polymer gel as in-vivo dosimetry technique during radiotherapy treatment.

The homogeneity and density of the filled dosimetric gel will be investigated after optimizing the 3D printing for a cuboid container for the gel bolus. A second part of the report will be dedicated to the gel dosimetry technique. A lot of research has already been done about PAGAT (polyarcylamide gelatine gel fabricated under atmospheric conditions) gel. Examples are the 'reproducibility study' and the 'Evaluation of radiochromic gel dosimetry and polymer gel dosimetry in a clinical dose verification' of J. Vandecasteele [11, 12]. This part is to see if it is possible to reproduce a dosimetric signal with the polymer gel when integrated in a printed PLA cuboid. Two runs were assessed in this work, each containing 2 printed cuboids. During the second run an intra-scan study and an inter-scan study were performed. An IMRT field will be used as delivery technique. The verification method of 3D printed bolus integrated with gel dosimetry will consist of a comparison with respectively the dose calculation by the treatment planning system (TPS) and the dose measured by EBT3 gafchromic film.

Chapter 2

Introduction

2.1 Radiotherapy work-flow

Principle

The principle of radiation therapy consists of the establishment of a uniform dose distribution in the desired target volume using multiple beams. A uniform dose distribution is defined by the ICRU as between +7% and -5% relative to a specified prescription point in the target volume [13]. This is carried out while keeping the dose as low as possible to the adjacent healthy tissues. The team consists of radiation oncologists, radiation physicists, radiotherapist, dosimetrist, nurse, psychologists and/ or social workers [14]. The general work-flow is illustrated in figure 2.1. Figure 2.2 represents the treatment room with the tools used for radiotherapy.

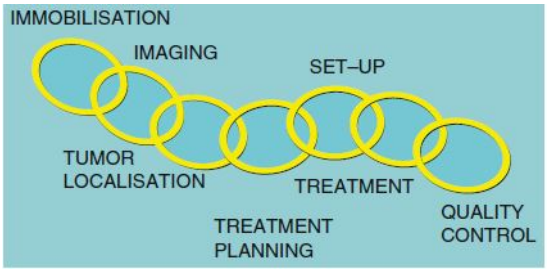

Figure 2.1: Involved steps in radiotherapy [14]

.

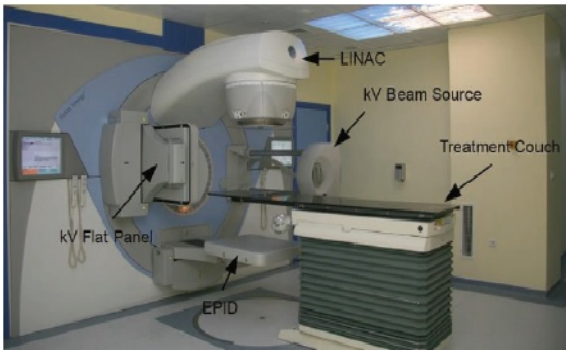

Figure 2.2: Example of a radiotherapy treatment room [14]

.

Data acquisition and simulation

The geometry of the patient is recorded using a diagnostic X-ray machine or in serial CT slices. Slice thickness depends on the region to be treated. The contour of the patient, tumour and target volumes are drawn on every CT slice. Organs at risk (OAR) must also be included in the drawn structures to make sure the dose constraint is not crossed. CT simulators are common in use to perform the required verifications and depend on immobilization, positioning, data acquisition and beam geometry determination [13]. Figure 2.3 shows a typical CT scnaner used for simulation and data acquisition.

Figure 2.3: Example of CT scanner used for data acquisition and simulation [14]

.

Immobilization and positioning Immobilization and positioning depend on the treatment position and precision required for the treatment. Examples of immobilization equipment are masks, knee supoorts,... Immobilizing is of importance because a slight movement or displacement can result in changes in treatment area and increase side effects [13]. A second important factor is the reproducibility of the position from simulation to treatment [13].

Imaging and tumour localization In this section the patient is positioned on the couch in a specific position corresponding to the type of tumour. Masks, plates, knee support structures may be used to accomplish this type of setting. After this the radiotherapy fields are determined and SSDs are calculated in function of the thickness of the patient. Flexible wires are used for palpable mass and drain sites and lead markers are applied for lateral epicanthal regions for head and neck.
If necessary contrast fluids can be given to the patient to enhance the image (IV or oral) [14].

CT simulation The radiotherapist manufactures the mask if necessary which is then inspected by the radiation oncologist. Lasers are available in the room to align the desired position of the ROI. Mostly three are located: craniocaudal, left and right lateral. Slice thickness and ROI is regulated by the radiation oncologist. It is advisable that reference points are to be marked permanently if no mask is used. After the CT images have been sent to the treatment planning room, the contours of the desired target volume are designated, external contours of the patient are mostly automatically generated [14].

Treatment planning

Several energies can be chosen from the linacs. These depend on the depth and type of the tumour. ICRU report No 50 and 62 are used to aid in the definition of these structures [13].

In conformal treatments organs at risk (OARs) and the delineation of the target volume come first. After this stage the treatment volume can be specified [14]. Medical physicians should also review the designed treatment planning before the application.
ICRU 50 and 62 are the most important reports involving photon energies. GTV, CTV, PTV and OARs require regulation to indicate a basis for several types of treatment and provide guidance during the planning protocol [13]. Figure 2.4 displays the different target volumes.

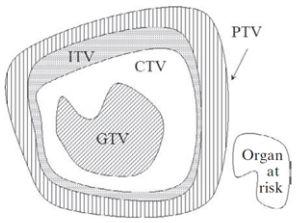

Figure 2.4: Involved steps in radiotherapy [13]

.

Gross tumour volume The GTV explains the extent and the location of the malignant tumour.CT, MRI and clinical examination are basic features which help to define the GTV [13].

Clinical target volume The CTV covers the GTV as well as the adjacent high risk surrounding tissues. Usually pathologists and radiologists are consulted to derive the fixed or variable margin around the GTV. Sometimes however the CTV is the equals to the GTV (i.e. prostate boost to gland) [13].

Planning target volume PTV contains the CTV with a fixed or variable margin due to uncertainties introduced by set-up, intratreatment variations and machine tolerances. However the specified margin does not account for penumbral and build-up regions. An additional margin is required during treatment planning and shielding [13].

Organs at risk These organs often have a low tolerance to radiation. In some cases that radiation beams from the planning treatment need to be changed in order to spare the organ at risk in question. During treatment planning these OARs are occasionally defined as structures to make sure the dose doesn't exceed the tolerances [13].

Set-up and treatment

Radiation oncologists should be present at the first set-up of the patient before irradiation and see the individual at fixed intervals during the fractions. It is important to position the patient as equally as possible to the simulation set-up. Electronic portal imaging devices (EPIDs) could also be used to verify the calculated dose distributions from the treatment planning system (TPS) [14]. The treatment room is also equipped with lasers to help to position the patient as reproducible as possible. Additionally the linac is equipped with a light field which corresponds

to the geometrical boundaries of the radiation field. These boundaries should be conform with 50% of the isodose curve with an accuracy of ±2 mm [15].

QA in radiotherapy

The accurate functioning of the equipment is the responsibility of the physician director. The QA team should consist of one physician, one physicist and a therapist. Quality assurance can be subdivided in daily, monthly and annual verifications [16].

Daily QA Rapid dosimetry equipment such as flat-panel detectors and ionization chambers are used to evaluate the output, flatness and symmetry, laser alignment, field size and ODI. Inconsistencies should be reported.

Monthly QA It is advisable to apply different verification techniques or cross-calibration of the daily QA to assess the monthly QA. This should be performed by a qualified medical physicist.

Annual QA These tests are checked with PDDs using water phantoms and calibrated NIST-traceable ionization chambers [16].

2.2 State-of-the-art high conformal radiotherapy treatment plans

2.2.1 Intensity modulated therapy: IMRT

Intensity-modulated radiation therapy (IMRT) is a state-of-the-art technique which involves the treatment of target volumes using an inhomogeneous radiation fluence. The purpose of this application is to align the intensity of the beam closely to the target volume. To accomplish this goal multiple radiation beams of varying sizes and varying intensities are used to improve precision and accuracy of the treatment. Consequently healthy tissues could be spared while allowing the tumour target volume to receive the clinical prescribed dose [17]. High-dose regions better align to the target volume by inverse treatment planning. An advanced computer algorithm is used for this task [18].

Planning The tools used for imaging, dose calculation, plan evaluation, QA and delivery are practically the same for IMRT as for current treatment procedures. As in conventional radiotherapy treatment a CT scan is taken to plan the GTV, CTV and PTV. Often 'pseudostructures' are applied during planning. These structures are created by the planners to set constraints in some crucial parts of the body where the dose needs to be limited. A very important aspect in IMRT planning is the consistency of the structures over the CT slices. If a single point is set somewhere it is not supposed to be, the inverse-planning algorithms will try to assign fluence to the selected region [17].

The next step is to place the isocentre which can be situated at the centre of the primary target or on a generic location (unlike conventional treatments). This can be done to overcome geometric restrictions. An example of this is mostly seen when wide targets are to be treated. The isocentre is then set to minimize the number of fields. An important factor here is the treatment

time which should be kept as low as possible. It is therefore necessary to find a compromise between the number of fields and irradiation time [17].

To optimize the plan hard and soft constraints as well as dose-volume based objective functions are required. Hard constraints specify limitations that the system must meet while soft constraints may be violated if necessary. A weighting factor is therefore assigned to tumour tissue and healthy tissue. This represents the importance of the specified constraint. For some organs, dose-volume histograms (DVH) are used to validate the treatment plan because the response of a tissue to radiation is a function of its volume [17].

Further optimization is described as an iterative process. After the TPS has done its calculations, the planner needs to evaluate outcome and change weighting factors if this would be favourable for the patient [17].

Treatment delivery IMRT treatments are delivered with the use of multileaf collimators (MLC). Nishimura and Komaki defined MLC as "small, individually motorized leaves that can be used to shape or modulate the intensity of the treatment field" (2014, p.23). The physical design and control mechanisms are very important features which determine the ability to form fields. Maximum leave travel, maximum field size perpendicular to the MLCs and the capability of interlocking MLCs from both sides are such factors [17].

Important aspects which should be considered are leakage through and scatter from the MLCs. These two factors are more important when using IMRT than conventional RT because IMRT uses relative small fields and thus the previous mentioned factors would contribute more to the target dose [17].

Sliding IMRT

In this treatment procedure the MLCs are moving while the radiation is continuously on. The shape of the gap in between the leaves is constantly varying due to the changing speed of the MLCs [17].

Step and shoot IMRT

This involves multiple static MLC segments, each segment having its own shape and weight. In between segments the beam is turned off. Using an algorithm, the entire dose distribution is divided in several steps while minimizing the number of steps and the MLC motion in between segments [17].

2.2.2 IMRT verification techniques

De Wagter C. proposed in his work a conceptual pyramid which represents the various levels of dosimetric QA in IMRT. When a new or modified technique is introduced, QA starts with 3D dosimetry of the entire treatment delivery. If however errors are detected when compared to the calculated dose distribution, QA verification can lower to the desired level until the discrepancy

is found. After this QA ascends back to the top [19, 20]. Figure 2.5 represents the discussed pyramid.

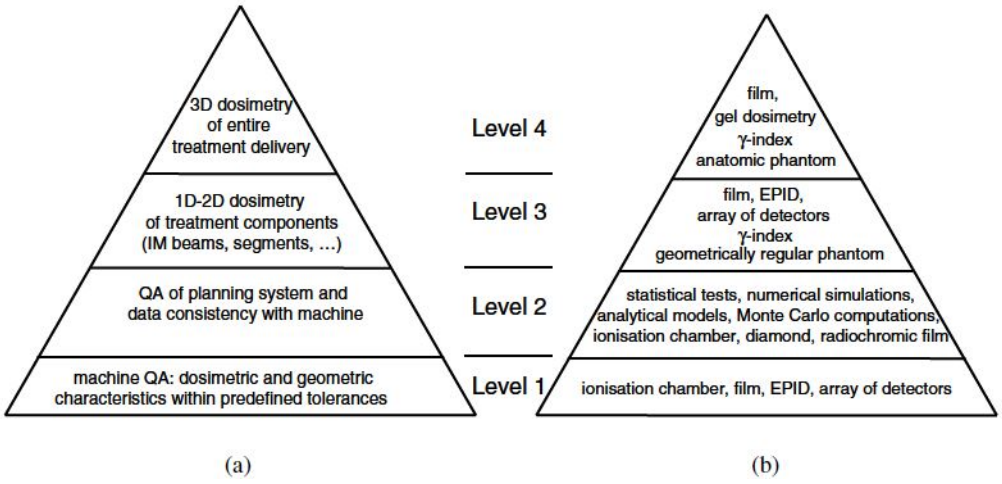

Figure 2.5: a) displays the conceptual pyramid for QA in IMRT. The two levels at the base could be for periodic QA procedures. A new or modified technique should start at the top and if there are errors detected QA verification must lower in level to be able to detect the discrepancy. b) represents the tools and methodology [19]

.

Ionization chambers

Calibrated ionization chambers with a good dosimetry protocol are regarded as the gold standard in radiation dosimetry. However when dealing with IMRT the size of the chamber does matter [19]. Errors in farmer type chambers could be 10% if chamber and field dependent corrections are ignored [21]. ICRU report stated a diameter larger than 0.3 cm already produces enormous errors [22]. This is due to the fluence perturbation effect and thus small volume chambers with high spatial resolution are proposed [19]. Therefore ICRU report no 83 recommends pinpoint ionization chambers. Other important factors such as chamber and cable leakage due to extended measurement times for IMRT must be accounted for [22]. Small volume chambers result in a standard uncertainty of 1.0-1.5% due to volume effects [22].

Radiochromic film EBT

In the clinic, radiochromic film dosimetry is a handy tool to verify the absorbed dose in a plane. The EBT3 film is used at the university hospital of Leuven.

Incident radiation which strikes the radiochromic film induces chemical reactions in the active radiation sensitive medium. This layer of the film is based on di-acetylene (C_4H_2). As can be seen in figure 2.6 thin microcrystalline monomeric di-acetylene emulsion is coated on a polyester film base [23].
At first the film is translucent before irradiation. Irradiation of these di-acetylene monomers which have highly unsaturated carbons forces a chain growth photopolymerization. A higher absorbed dose produces a darker blue color. One great advantage is the self-developing characteristic of the radiochromic film. After being irradiated the polymerization goes on for several

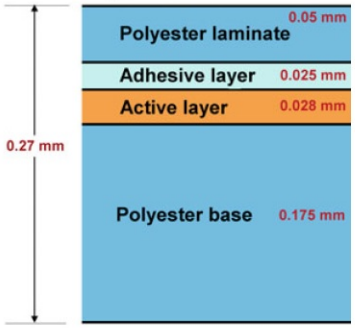

Figure 2.6: Layer distribution EBT2 radiochromic film [23].

hours depending on the batch. Radiochromic film is also nearly water-equivalent, doesn't have a dose rate dependence, provides excellent image resolution and can be cut in several shapes in daylight. Nevertheless humidity and ambient temperature during irradiation should be controlled strictly. The film is also sensitive to ambient fluorescent light and sunlight [23].
The absorbed dose is proportional to the darkening. Therefore read-out consists of a device such as a flatbed scanner. Using the calibration function, the amount of light transmitted through the film is then a direct measure of the absorbed dose [23]. An important feature is its time-dependence between irradiation and read-out [22]. The currently used EBT3 batch needs 48 hours of post-polymerization before read-out.

The incident light of the flatbed scanner is split into three primary colors: blue, red and green. Extraction of the red color is quite common because the absorption spectrum of EBT films is maximal in the red color region of the visible light spectrum [19].
The general characteristics of the EBT batch can be seen in table 2.1. According to the manufacturer EBT3 films are nearly equal to EBT2 films in performance and construction. Adaptations involve the feature of a symmetric construction and anti-Newton ring artefacts coating. Symmetric construction should improve scanning procedure in a clinical setting [24].

Table 2.1: General characteristics of the radiochromic EBT film. This table comes from "Radiation physics for medical physicists", third edition by E.B. Podgorsak [23], p.810.

Characteristics	EBT gafchromic
Radiation sensitive medium	Di-acetylene C4H2 monomer
Radiation induced process	polymerization of di-acetylene monomer into polymer
Post-irradiation film processing	NO
Darkroom required	NO
Film spatial resolution	High
Water equivalence	YES
Signal low-energy dependence	Slight
Dose rate dependence	NO
Visible light sensitivity of unexposed fim	NO
UV sensitivity of unexposed film	YES
Allows direct water immersion during irradiation	YES

All of the above mentioned characteristics makes EBT3 film a good evaluation for high quality dosimetry in IMRT. EBT films can be used in pre-treatment patient specific QA when new methods are implemented or in complex cases. A gamma map analysis using a combination

of distance to agreement and dose difference is then performed to analyse the measured and calculated dose distributions [19].

Electronic portal imaging devices: EPIDs

Originally EPIDs were constructed to obtain megavoltage (MV) images during treatments. This was done to minimize set-up errors. However the acquired data from the image can be used for determining dose information in a plane. According to Alber M. *et al.* EPIDs could verify the leaf position, check the leaf sequencing and measure mechanical and dosimetric performance of the treatment [19].

Two types of techniques can be chosen: transmission and nontransmission dosimetry. Transmission measurements are done using a patient or a phantom. There are also two approaches: forward and backward approach. The first approach compares the measured dose distribution with the calculated data coming from the TPS whereas the latter reconstructs the dose within the patient or phantom from the acquired data in the EPID [25].

Some characteristics need to be verified before an EPID could be used as a dosimetric tool. Alber M. *et al.* specified these factors as the dose-response curve, temperature, dose rate and dose per pulse dependence, reproducibility of the signal and response variation with gantry rotation angle. Amorphous silicon (a-Si) EPIDs exhibit an almost linear response and are quite fast [19]. A-Si type EPIDs stops photons and sends visible light to phototransistors which convert this into a current which is integrated by a capacity.
Two main problems concerning EPIDs are also discussed in this article: ghosting and energy dependence. Ghosting is defined as additional signal after the irradiation has ceased. In the case of IMRT some problems arise because individual pixels are irradiated in a different way making it difficult to take the missing signal into account. The second problem (energy dependence) is a result of the high Z materials from which an EPID is constructed. This could create an over-response in the low energy region [19].
Nowadays there are several solutions for the previous addressed problems making it possible to evaluate measured and calculated dose distributions. In IMRT cases, EPIDs are replacing film dosimetry to perform pre-treatment verification. Pecharromn-Gallego R. *et al.* sums several advantages in their article: ease of use, fast data acquisition, high spatial resolution, digital format of images, sufficiently large fields of view and an accurate dose-response relationship [25].

2.2.3 Volumetric modulated arc therapy: VMAT

Volumetric modulated arc therapy is an innovative form of IMRT. The principle handles the fact that the radiation dose can be accurately and efficiently delivered in a single gantry rotation of 360°. A constant dose rate or variable dose rate can be chosen. VMAT can be more advantageous in treatment time and in reduction of MUs for a given fraction [26].

2.2.4 Proton therapy: PT

As earlier explained external beam therapy continuously aims to improve tumour target coverage while sparing the surrounding healthy tissue. Protons have a specific advantage over conven-

tional photons: the Bragg peak [27].

This peak consists of an entrance plateau followed by a sharp peak (figure 2.7). This phenomenon is as a consequence of the number of particles which decrease and the increase of the stopping power (energy released per unit length) in depth. The latter depending on the inverse of the speed of the particle squared [27].

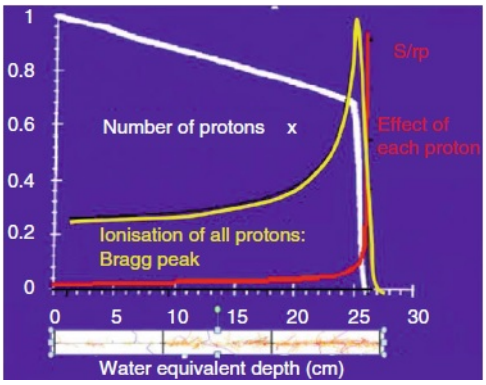

Figure 2.7: Proton (around 200 MeV) depth dose curve in water (yellow). White represents the number of particles and red the stopping power. Values on Y-axis stand for the fraction of maximal value [27]

.

Subsequently multiple proton beam energies could be used to compose a "spread out Bragg peak" (SOBP) (figure 2.8) resulting in a flat, high dose region that would cover the target volume adequately [18].

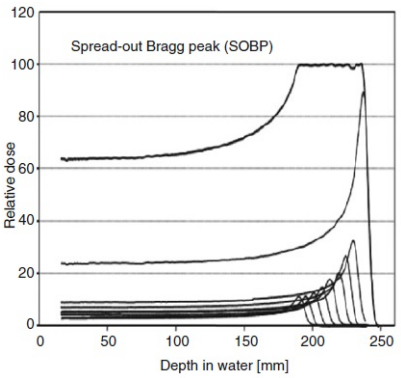

Figure 2.8: Spread out Bragg peak [27]

.

Obvious advantages of the previous mentioned characteristics of protons are the flat homogeneous dose region, high gradient after and, above all nearly no dose after the target. Nevertheless there is a high entrance dose, increased lateral penumbra in depth, the presence of a neutron dose near the target and the uncertainty in range [27].

Current relative biological effectiveness (RBE) is set at a value of 1.1 which is currently used at proton treatment facility centres because of the difference between protons and photons. The RBE depends on local linear energy transfer, dose and tissue α/β ratios [28]. The linear energy transfer increases with decreasing proton energy near the end of their penetration range [18] and

the tissue (α/β) is often not known exactly [28]. This indicates uncertainties in the definition of RBE for protons and influences the interpretation of proton dose distributions [28].

The sharp dose falloff results in a better tumour target coverage but a worst case scenario could be partially or completely missing the target due to a slight error or unexpected shift in the positioning of the patient [27]. In-vivo dosimetry could evaluate the successfulness of the treatment.

2.3 In-vivo dosimetry

In external beam radiation therapy (EBRT) in-vivo dosimetry (IVD) is a technique where a detector is commonly placed onto the skin or near a part of the patient where assessment of the dose is necessary. The measured data can then be linked to the dose deposited inside the patient. IVD is crucial there where QA checks or pretreatment measurements cannot detect potential discrepancies [6].

It is important during radiotherapy that the prescribed dose is given to the target volume. Underdosage may result in tumour control failure whereas overdosage may cause some serious complications. IVD would be able to highlight dose errors and thus provide the possibility to take corrective actions resulting in reducing harm to the patient [29].
Counterarguments consist of expensiveness and time consuming factor. Investments in the implementation of IVD would probably result in less funding for new upcoming developing techniques. Another problem is that most common IVD methods (mostly point-measurements) do not have the capability of verifying modern applicable fields such as IMRT and VMAT [29].

Two kinds of detectors are available to do IVD: real-time and passive detectors. A brief explanation concerning the most common detectors will be discussed.

2.3.1 Types of detectors and their characteristics

Real-time in-vivo dosimetry

Metal-oxide semiconductor field effect transistors (MOSFETs), diodes, plastic scintillation detectors (PSD) and EPIDs will be briefly reviewed. Mijnheer B. *et al.* distinguished different IVD detectors with each their advantages and disadvantages [6].

MOSFETs MOSFETs are field effect transistors rely on the change in threshold voltage which is a linear function of the delivered dose. Customarily the integrated dose is measured after irradiation. Advantages of MOSFETs are its spatial resolution without build-up cap and its little beam attenuation (small size detector). The latter making it very useful to do in-vivo dosimetry. It however has an energy dependence, angular dependence and dose rate. The response of the detector also changes with temperature and with accumulated dose and therefore recalibrations are necessary. Disadvantages are its lifetime which is rather short and the high cost.

Diodes Diodes have some great assets. These detectors are simple, exhibit a high sensitivity, are reliable and robust. Nonetheless if a build-up cap is used for in-vivo measurements the diode is dependent on dose rate, irradiation angle and energy of the beam. Other factors that must be taken into consideration are the varying response with changing temperature and the altering sensitivity with large accumulated doses resulting in the need for recalibration.

Plastic scintillators Plastic scintillation detectors (PSDs) are composed of organic molecules in a polymerized solvent. When radiation strikes light is emitted and detected by a photodetector and optical fiber. The absorbed dose is proportional to the emitted light of the scintillator. Advantages are water equivalence of the detector, energy independence and linearity of the dose. Light emission is established in the order of nanoseconds resulting in the capability to do real-time measurements. It has an excellent spatial resolution due to its small finite size. A disadvantage is the radiation induced light such as Cerenkov and fluorescence phenomena in the optical fibers.

EPIDs EPIDs were already discussed in section 2.2.2. A great benefit is that this technique is non invasive and has the possibility to capture 2D and 3D dose information.

Passive in-vivo dosimetry

TLDs Thermoluminescence detectors absorb energy in metastable states. When the powder, chip, rod or ribbon is heated the energy is discharged in the form of light. This is proportional to the absorbed energy. TLDs are energy dependent and this must be taken into consideration, especially in de kV range for brachytherapy. It is recommended to calibrate the TLD in the beam which will be applied. TLDs must be annealed after use to erase the residual signal. A disadvantage is the fading of the obtained signal which occurs after irradiation. Their use is also labour intensive and has.

Radiochromic film EBT Radiochromic film was already discussed in section 2.2.2. It is mostly used for skin dose measurements, total body irradiations (TBI) and total skin electron irradiation (TSEI).

2.3.2 Implementation IVD in a clinical setting

A first requirement is that the system needs to be tested under well-controlled conditions. The actual treatment must be simulated as good as possible. Semi anthropomorphic phantoms and regular slab phantoms are often used to mimic the patient. Additionally fiducial markers can also be placed on the phantoms to evaluate the set-up of the patient and detect a potential error.
In a second step protocols should be written. The use of the detector equipment, the IVD measurement and reports for evaluating the measurement should be available [6].

2.3.3 In-vivo dosimetry for IMRT and VMAT

Point detectors are often used to verify the treatment. Mijnheer B. *et al.* describes that MOSFETs, TLDs, diodes are applied for IMRT head and neck treatments. They could be placed on the skin to measure entrance dose. EPIDs are becoming an important asset for dosimetrical

purposes. They could provide 2D and 3D dosimetrical information.
The author concludes that 2D and 3D verification techniques for IMRT and VMAT are a necessity because some centers cannot achieve the acceptance criteria [6]. Interested readers can read these results and conclusions in the following articles: [30, 31, 32, 33, 34, 35, 36, 37].
3D in-vivo dosimetry will be an important asset for high conformal treatment plans such as IMRT, VMAT, proton and ion beams. It will become an important tool not only for verifying the absorbed dose given to the patient but also for plan adaptation [6].

2.4 Three dimensional polymer gel dosimetry

Quality assurance (QA) determines the consistency and quality of the radiotherapy treatment. In this process a lot of methods are implemented to assure an adequate quality and thus minimalization of errors. There are already a lot of detectors on the market for dose verification, each having their advantages and disadvantages.
Three dimensional dosimetry is recently becoming more popular in routine dose verifications for certain treatment procedures, i.e. Intensity Modulated Arc Therapy (IMAT) or Image-Guided Radiotherapy (IGRT). Here, gel dosimeters may offer a solution over the limitations of 3D systems which use detector arrays of diodes or ionisation chambers [8].

2.4.1 Polymer gel dosimeters

Principle of a PAGAT polymer gel dosimeter

The principle of a gel dosimeter is based on the radiation induced polymerisation of acrylamide (Aam) with a crosslinker N,N'-methylene-Bis-acrylamide (Bis) in a gel matrix. This polymerisation reaction between Aam and Bis starts due to the radiolysis of water. The added gelatine takes care of spatial stability. A disadvantage is that the atmospheric oxygen also forms radicals during irradiation. These radicals have the ability to stop the polymerization process between Aam and Bis. Because of this, oxygen is removed during the fabrication process. THPS (tetrakis (hydroxymethyl) phosphonium sulphate) is an antioxidant which binds to the atmospheric oxygen in a complex. All of these factors contribute to the creation of the PolyAcrylamide Gelatin gel fabricated at ATmospheric conditions, i.e. PAGAT gel [8].

PAGAT gel dosimeter

The PAGAT gel consists of two monomers Aam and Bis, deionised water and THPS (figure 2.9). This is added to remove the atmospheric oxygen [8].

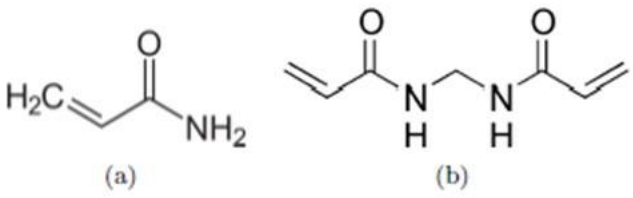

Figure 2.9: a) Aam and b) Bis [8].

When the gel is irradiated by high energy X-rays, water molecules dissociate in highly reactive radicals and ions ($OH^{\bullet}$ and $H^{\bullet}$). The polymerisation reaction is then induced by the reaction of the previous mentioned particles with available monomers or with an already formed polymer. These reactions will continue untill termination of the chain occurs. Vandecasteele Jan discussed in his PhD the most important termination factors: the reaction of two initiating radicals resulting in a stable initiatior, disproportionation during which a hydrogen atom is transferred from one polymer radical to the other which corresponds to an oxidation of the donor and a reduction of the acceptor, the transfer of the active radical group to other molecules and reactions of the growing polymer with the gelatin matrix.
The function of the gelatin matrix (figure 2.10) is to spatially fix the polymer chains. A 6% w/w concentration in a PAGAT gel dosimeter gives it just the right mechanical firmness and dose sensitivity [8].

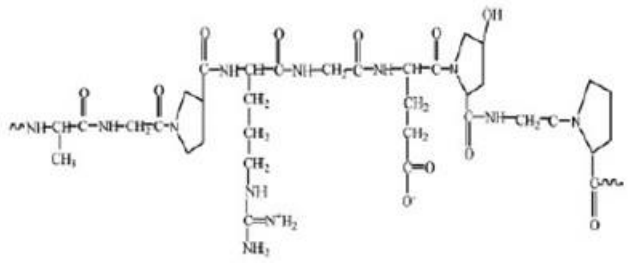

Figure 2.10: Molecular structure of gelatin [8].

According to several studies, the PAGAT gel contains the lowest temperature dependence in storage and irradiation. On top of that, it has no dose rate dependence [12].

Dosimeter read-out: MRI

The absorbed dose inside the gel dosimeter is indicated by the magnitude of polymerisation. This effect strongly influences the NMR spin-spin relaxation rate (R_2), the inverse of the relaxation time T_2.
MR imaging uses hydrogen atoms for image generation. This is because of their high magnetogyric ratio and two possible spins: $I = \pm\frac{1}{2}$ which result in only two possible orientations of the spin: parallel with the external magnetic field or antiparallel [38].

Three different proton pools can be found in an irradiated gel dosimeter: one associated with the free water molecules and small momomers, another in the gelatin matrix and at last in the created polymer chain upon irradiation. In case of the latter, the protons can be found in the chain itself and in the bound water molecules.
After being irradiated the third pool will increase while the first pool (the monomers) decreases. This means that the mobility of the protons is decreased, thus the T_2 also decreases. The relaxation times of the protons are large when compared to their lifetimes. This means that the relaxation rate coming from the MRI scan will be a weighted average between the three proton pools.
The R_2 parameter is determined by specific imaging sequences. These are acquired to calculate the magnitude of the polymerisation inside the gel. Eventually R_2 maps are accomplished from T_2-weighted images.

In the end a good calibration strategy is required to obtain the desired dose maps. Mostly a series of calibration phantoms is used. These phantoms are all from the same batch and irradiated to different well-specified doses [8]. A calibration curve is attained by plotting the mean R_2 values from the cross-sections of the calibration phantoms to their well-defined doses. The following equation specifies a mono-exponential function which is backed by the analysis on monomer consumptions [39].

$$R_2 = R_{2,sat} - \Delta R_2 \cdot e^{-\alpha \cdot D}$$

Where $R_{2,sat}$, ΔR_2 and α are the fitting coefficients.

2.4.2 About 3D dosimetry in the clinic

During IMRT (Intensity Modulated Radiotherapy) and IMAT treatments, the dose is delivered dynamically to the patient. This means multiple beam defining parameters such as dose rate, radiation fluence and shape of the beam will vary continuously. If the treatment is more precise, then the procedure will be more sensitive to uncertainties.
Therefore a system is required that can link accumulated errors to their clinical relevance. If an error is detected, it should be possible to assess in which stage of the procedure this occurred to improve the QA system [8].

2.4.3 Literature review of depth dose measurement and IMRT dose verification

Vandecasteele and De Deene published articles concerning the evaluation of polymer gel dosimetry in a clinically dose verification. Materials and methods, results and discussion can be found in "Evaluation of radiochromic gel dosimetry and polymer gel dosimetry in a clinical dose verification" [12].
It was found that a very strict protocol is needed to be able to reach a clinical acceptable level of accuracy of absolute dose within 5%. This somewhat limits the use of this gel in clinical practice. Nevertheless it is a crucial feature to validate more and more complex treatments [12]. However to attain the 5% accuracy a dedicated temperature stabilizing protocol is needed [12]. First of all a similar cooling trajectory for calibration vials and phantoms is of utter importance. The following section 2.4.4 will explain this phenomena more in detail. Additionally the temperature difference during MRI read-out between the phantom and the calibration phantom causes an overestimation of the dose which can be significant. Due to this fact, it is advised that the polymer gel dosimeters are placed in a water container with active temperature stabilization to within 0.2°C. This procedure also limits the occurrence of artefacts concerning the magnetic fields [40].
To achieve this water perfused thermal pads were attached to all the phantoms which were resting in a water bath doped with GdDTPA at a fixed temperature. Due to the fact that 0,25 °C can already result in a dose deviation of 2,25 %, the author concluded that this method may not be adequate enough to keep the temperature differences at bay [12].

Other inconsistencies were observed due to the finite size of the used head coil during MRI read-out. The transmit-receive CP head coil has a finite volume where the nuclei are equally excited i.e. the flip angle. This means a change in the positioning of the phantom results in a

different equally excited volume where the accuracy is approximately ±4% [12].

2.4.4 Factors causing dose errors

Influence of the cooling rate on accuracy

De Deene *et al.* subjected different series of the same batch to diverse thermal storage conditions after fabrication of the gel. It was concluded that the dose-R_2 sensitivity was slightly smaller for actively cooled gel compared to one stored at room temperature. The results of the calibration curves showed a maximum dose error of 7% at 10 Gy for a temperature offset between calibration vials and the phantom of 18°C for about 7 h. If bigger phantoms are actively cooled down, a temperature difference can occur between the middle of the phantom and the edge. The solidifying process of the gel may disrupt convection currents which are a result of temperature differences inside the phantom. The use of a large water tank is therefore advised to cool down the phantom and calibration vials equally and slowly to room temperature [41].

It was also found that higher measured R_2 values correspond with an exposure to a colder temperature. A later study conducted by Vandecasteele and De Deene (2013b) observed a dose deviation of 6% with an offset of 8°C for 14 h (30 h post-irradiation measurement). Another conclusion of this article stated a changing dose deviation with post-irradiation time. These results are assumed to be a consequence of the adjusting macromolecular environment (THPS and gelatin) after irradiation [42].

Calibration method

An R_2-dose plot is used where mean R_2 values are represented as a function of the dose. These points show correspondence with a mono-exponential curve where $R_{2,sat}$, ΔR_2 and α are the fitting coefficients.

$$R_2 = R_{2,sat} - \Delta R_2 \cdot e^{-\alpha \cdot D} \tag{2.1}$$

Other relations such as the slope which is the derivative at 0 Gy (2.2) and the R_2 increase (2.3) (δ R_2, between 0 and 12 Gy) can also be used to intuitively form a fast global image. In the following equations $R_{2,0}$ is the y-axis intersection and $R_{2,sat}$ the saturation R_2 value.

$$slope = \Delta R_2 \cdot \alpha \tag{2.2}$$

$$R_{2,0} = R_{2,sat} - \Delta R_2 \tag{2.3}$$

Vandecasteele and De Deene (2013a) proposed in their work some calibration methods to improve the accuracy of the measured dose.
A first method depends on the linear renormalization of the calibration function. Here, two regions of interest (ROI) are chosen from the planned dose distribution. One is selected from the low dose region, the other from the high dose region. These ROIs are then used to determine the measured R_2 values. A first step is to save the α value from equation 2.1.
Hence, the new coefficients (Δ R'$_2$ and R'$_2$) could be calculated from equations 2.4 and 2.5 and combined with α from equation 2.1.

$$\Delta R_2' = \frac{R_{2,2} - R_{2,1}}{e^{-\alpha_1 \cdot D_2} - e^{-\alpha_1 \cdot D_1}} \tag{2.4}$$

$$R_{2,sat}' = R_{2,1} - \Delta R_2' \cdot e^{-\alpha_1 \cdot D_1} \tag{2.5}$$

Here $R_{2,1}$ and $R_{2,2}$ correspond to the low-dose and high-dose region respectively. D_1 and D_2 are planned dose values that are linked to $R_{2,1}$ and $R_{2,2}$. In this way renormalization occurs with data from the dose distribution which is actually being verified. Additionally the doses could be validated by an independent dosimeter and as a consequence this technique could still be used as an independent dose verification technique [11].

Long term response stability

An experiment performed by Vandecasteele and De Deene (2013a) showed that the intuitive parameters described in the previous paragraph change slowly in time after irradiation. Hence read-outs were performed at 6, 30, 54 and 95 h post-irradiation on a total dose of 12 Gy, values are listed in table 2.2. As can be seen the maximum dose deviations are 14.6%, 1.4%, 4.5% and 4.3% for 6 h, 30 h, 54 h and 92 h respectively [11].

Table 2.2: Maximum differences in intuitive parameters in absolute values and relative to the mean value. Maximum dose difference is a result of calibrating the same measured R_2 values with the most diverging calibration curves, copied from [11],p.27.

Calibration parameters at	6 h	30 h	54 h	92h
Mean slope ($\cdot 10^{-2}$s^{-1}Gy^{-1})	6.48	7.24	7.20	7.41
Δslope$_{max}$ ($\cdot 10^{-2}$s^{-1}Gy^{-1} (%))	0.499 (7.7%)	0.221 (3.1%)	0.079 (1.1%)	0.166 (2.2%)
Mean intercept (s^{-1})	1.06	1.22	1.29	1.26
Δ Intercept$_{max}$ ($\cdot 10^{-2}$s^{-1} (%))	3.12(2.9%)	0.84(0.7%)	1.52(1.2%)	1.33(1.0%)
Mean saturation (s^{-1})	1.875	1.993	2.105	1.979
Δ sat$_{max}$ (s^{-1} (%))	0.172(9.2%)	0.247(12.4%)	0.233(11.1%)	0.174(8.8%)
Δ D$_{max}$ (Gy (%))	1.75(14.6%)	0.164(1.4%)	0.541(4.5%)	0.517(4.3%)

The change in slope and intercept were calculated to be $0.00205 \cdot$s^{-1}Gy^{-1}h^{-1} and $0.0116 \cdot$s^{-1}h^{-1}. The R_2-dose stability depends highly on the diffusion of monomers and radiolytic water molecules. The observed changing slope in the linear part of the R_2-dose curve is due to the post-polymerization of the monomers. Variations in the intercept however are a consequence of the continuation of the gelation process of gelatine. The study of De Deene (2000) concluded that after approximately 12 h the post-irradiation polymerization ends while the gelation process continuous for several days [43].

Oxygen effects

As already explained in the previous section 2.4.1 atmospheric oxygen needs to be removed from the solution during the fabrication process because of its capability to inhibit the polymerization process [8].

Infiltration of oxygen prior to irradiation results in large fluctuations in R_2 values. These regions showed an inhibition of polymerization. Another consequence of oxygen diffusion is the dehydration of the gel. A steep increase of R_2 values was observed in regions of dehydration. On

the other hand post-irradiation oxygen diffusion show no notable difference in R_2 values within the uncertainty of the measurement at larger distances [42].

Temperature differences during read-out

Most of the time the temperature recorded inside the scanner bore is higher than the surrounding area. A measured difference of 2°C is common. Results of previous experiments demonstrated that absolute mean dose deviations could not be reproduced, however the sign was (overestimation). The main contributing factor reported was the higher temperature of the calibration phantoms in comparison with the volumetric phantom [11].

A later study produced a dose deviation of 2.58% compared to ion chamber measurements. It should be stated however that here temperature-controlled conditions were present, i.e. a cylindrical recipient doped with GdDTPA (avoid imaging artefacts caused by the motion of circulating water, T_1 and T_2 smaller than 60 ms) connected to a temperature-controlled water bath [40].

It was proven that a temperature difference of 1°C between calibration and experimental phantoms produced an uncertainty of 9% at 10 Gy with a 6% monomer concentration. Also a doubling of the dose showed a doubling in dose deviation.

The maximum dose given to a PAGAT dosimeter should be under 15 Gy, otherwise spatial dose-integrity from diffusing monomers cannot be guaranteed [40].

It must be noted that the measured R_2 value is not only dependent on the temperature but also on the monomer concentration. Figure 2.11 represents the effect of temperature on the measured dose during read-out for a 5% and 6% monomer concentration solution.

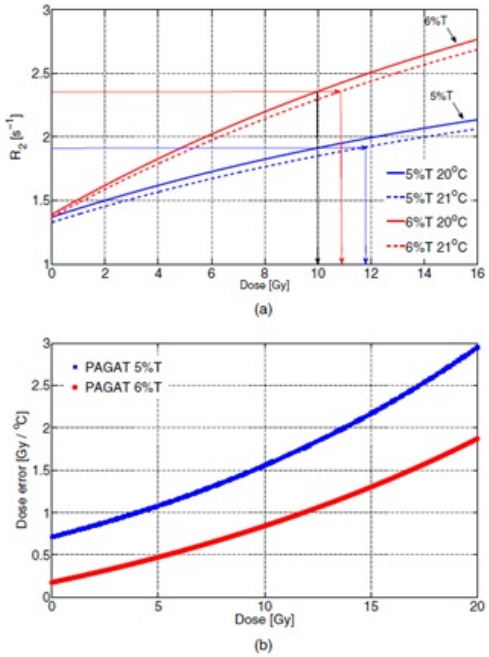

Figure 2.11: Effect of temperature during MRI read-out for a 5% and 6% monomer concentration. a) The arrows indicate dose deviations for 1°C at 20°C. b) Dose error per °C as a function of the dose for a 5% and 6% monomer concentration [40].

Dose overshoot

Dose overshoots may occur near the edge of high dose gradients. This is a consequence of the long-lived polymer radicals. However these overshoots should decrease with post-irradiation time. A maximum overshoot at 12 h after irradiation was measured after which it started to decrease [44].

Another research conducted by Vergote *et al.* also reported dose overshoots near high dose gradients. This is supposed to be due to temporal instabilities after irradiation of the gel. Another reported fact is overshoot in the penumbra width (region between 10% and 90% of the dose). An increase in penumbra width illustrated a decrease in the magnitude of overshoot [45].

2.5 Additive manufacturing

2.5.1 Printing technique

3D printing or rapid manufacturing has gained a lot of popularity in recent years. This is due to the high flexibility in shaping the desired object and a wide range of materials which are already available on the market.

The 3D printer located at the department of radiotherapy and oncology at UZ Leuven is a Felix pro 2 printer, desktop size, which uses the fused deposit modelling (FDM) production technique. Here, a thermoplastic filament is fed to a temperature-controlled extrusion head. This melts the material to a semiliquid state and deposits it on temperature-controlled bed. After deposition on the bed, the thermoplastic cools down and hardens. This results in a 3D model built layer by layer. The filling degree of these objects can be varied freely. Support structures are often required when dealing with printing structures with overhanging geometries because of the hardening time of the thermoplastic. The use of dual-nozzle configurations can be advantageous: the support structures can be printed in water-soluble material (i.e. PVA) [46].

However the FDM printing technique scores poor in terms of printing speed, accuracy and surface finish. Nevertheless it is cheap and easily available which makes it common in use [46].

2.6 A 3D printed bolus integrated with dosimetrical properties

2.6.1 Bolus in radiation therapy

Megavoltage photon beams are often used during radiotherapy. The irradiation of a person or phantom results in an absorbed dose which varies in depth. Many different parameters such as beam energy, depth, field size, source to surface distance and beam collimation system contribute to these variations. The depth dose curves are mostly measured by ionization chambers which move along the central axis of the incident beam [47].

At the beginning of the PDD curve, there is a build-up region. This becomes more visible when higher energies are used. The maximum depth dose given by low energy bundles is near the surface while higher energies tend to have a deeper depth of maximum dose. As can be seen

for example in figure 2.12 there is a dose build-up region between the surface and the point of maximal dose. This phenomenon is also called the build-up effect [48].

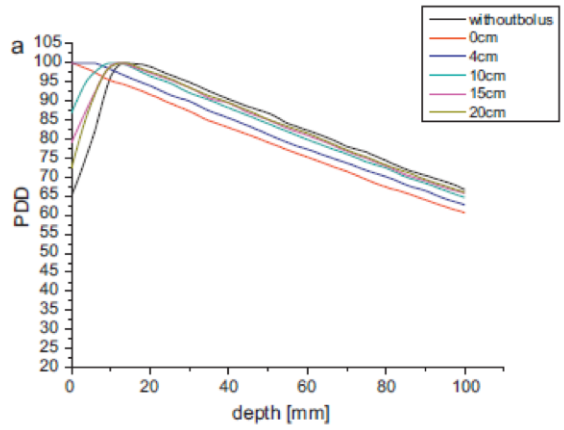

Figure 2.12: PDD for a 6 MV photon beam and field size 10 x 10 cm for several bolus surface distances [49].

The skin sparing effect is not favourable when dealing with tumours near the surface because of the reduced effective dose. A build-up bolus is a tissue-equivalent material which is placed directly onto the skin of the patient and is thick enough to provide a satisfactory build-up resulting in a maximal dosage to shallow tumours. This phenomenon is illustrated in figure 2.12 where no build-up region can be seen if the bolus is directly applied on the skin (orange curve). Another quality of the bolus is to be able to create a flat surface normal to the beam in cases of irregular contours of the patient which enables a more uniform dose distribution [47].

Bolus material criteria proposed by Chang *et al.* are tissue equivalent, to be made of safe materials approved by FDA, to be convenient for daily use and not to be altered in appearance after high dose of irradiation [50].

Examples of commercially available boluses are paraffin wax and superFlab (figure 2.13). The latter is a proprietary synthetic gel which does not suffer inelastic strain from normal stresses. Nevertheless it is used a lot to deliver the maximal dose to superficial tumours because it conforms well for simple geometries, maintains uniformity thickness and elastic properties. It has a specific gravity of 1,02 [51].

Figure 2.13: superFlab bolus [51].

2.6.2 In-vivo gel dosimetry and 3D printed bolus

The compatibility of these boluses with HNC has proven to be difficult because of the pronounced irregularities situated in these areas. The superFlab will not be able to align closely with the skin resulting in air gaps. In combination with the thermoplastic mask, the comfort of the patient will also decrease.
As earlier explained in the section 1.2 the difficulty of complex structures in the head and neck region could be overcome by customizing the bolus to the patient. A primary concern when applying a bolus to the skin is to avoid air gaps in between them. Butson J. M. *et al.* concluded in their research that when a gap of 10 mm between the bolus and skin is applied, 90% of the maximum dose is delivered [48].

As discussed in section 2.3 mostly point detectors are used to do in-vivo dosimetry. Leman J.L. concluded in her article that current IVD methods are not satisfactory enough to validate the complex treatments (IMRT, VMAT) [29] while Mijnheer B. *et al.* described the need for 2D and 3D in-vivo dosimetry (section 2.3.3) for IMRT and VMAT conformal treatments [6]. These articles indicate the need for an integrating IVD technique which could record the complete fluence of the applied field. These are the most prominent reasons why the feasibility of a 3D printed bolus integrated with polymer gel must be assessed.

Chapter 3

General materials & methods

3.1 3D printing

A Felix pro 2 printer is available at the department radiotherapy and oncology at Leuven, Gasthuisberg. This printer uses the fused deposit modelling (FDM) production technique. PLA was selected as the thermoplastic filament. The program FELIXbuilder provides several parameters which can be adjusted to obtain the desired print. The most important characteristics will be discussed in the next few paragraphs.

Contours The 'number of contours' sets the number of contours which will be used by the model. The contour overlap represents the amount of overlap when a contour is closed. The term 'before infill' refers to the fact that the contours will be printed before the infill. The offset is used to set the distance between contour lines in a % of the default wire width (0,4 mm). Print speed factor and extrusion factor were already specified by the manufacturer [52].

Up skin/ Down skin (bottom and roof) The number of layers specify the number of layers which will be printed in an up skin or down skin. Line distance stands for the distance between the lines as a percentage of the default wire width (0,4 mm). Infill overlap determines the overlap between bottom/roof with the inner contour. The angle at which the bottom or roof will be filled can also be chosen. The angle of the next layer of infill with respect to the previous one is set with 'angle increment'. Again print speed and extrusion factor were specified by the manufacturer [52].

Start point relocation Start point relocation gives the opportunity to choose at which point of the layer the nozzle will begin.

3.2 Gel dosimetry

The process of fabrication, irradiation and MRI read-out of the PAGAT polymer gel is a concatenation of different elements, each introducing it's own uncertainties. The first one being the establishment of a similar cooling rate between phantoms and calibration vials [41]. This problem could be solved by placing both in a water tank set at the temperature of the gel just after fabrication which is 32 °C. A second uncertainty is introduced by the stabilizing process

after being irradiated. The gel needs to rest for about 12 hours before the MRI read-out [44]. A third uncertainty is introduced during the MRI read-out where an offset in temperature between calibration vials and the gel within the printed cuboids could result in a dose deviation. A dedicated read-out procedure to minimize this effect is desirable [11].
Because of this reason a protocol was written based on several articles, for example [8]. The protocol can be found in the appendix.

The next few sections will discuss the procedure which is followed to obtain a dosimetric signal from the PAGAT polymer gel. Also, the set-up for the reference gafchromic film (EBT3) will be explained. This order is used for the preliminary study as well for the second run.

3.2.1 Fabrication of the gel

The gel was fabricated as described in De Deene *et al.* [53]. The following procedure explains the fabrication of 1 l polymer gel.
First 60 g of gelatine was added to 440 ml of deionized water at room temperature after which the solution was slowly heated to a temperature of 45°C. The gelatine solution should not be heated to temperatures higher than 50°C because this would result in a shorter network of gelatine chains. This means that the water would be less mobile and that the background relaxation value R_2 during read-out would be higher. Eventually a lower ratio of signal to noise would be observed.

While the gelatine solution is slowly heated, 30 g of acrylamide (Aam) was dissolved into 440 ml of deionized water (room temperature). Aam has a good solubility. Next the crosslinker N,N'-methylene-Bis-acrylamide (Bis) was added to the acrylamide solution while constant stirring at full power. The mixture was slowly heated to a temperature of nearly 60°C after the Bis was added. At this temperature the solution became transparent.

Both solutions were allowed to cool down to a temperature of 45°C before mixing. At last THPS (5mM) had to be added to the mix to bind to the dissolved oxygen in the mixture. Oxygen has the ability to inhibit the polymerization process upon irradiation and thus has to be avoided as much as possible. A crucial aspect of this part was the temperature of the solution which had to be 32°C before the THPS could be added. Figure 3.1 displays the set-up. It should be noted that the entire experiment had to be done beneath the fume hood with protective clothing (mask, gloves, glasses and lab coat). One must always keep in mind that Aam is neurotoxic and carcinogen while Bis causes irritations.

Figure 3.1: The set-up: gelatine solution (left) and acrylamide solution (right).

3.2.2 Storage

The gel was poured into the manufactured 3D cuboids and calibration vials using a syringe of 60 ml. These were placed into a plastic water tank at 32°C to ensure a similar cooling trajectory. It has been shown that the obtained R_2-dose response depends on the cooling history and may result in a certain dose difference [41]. The plastic tank was then placed in a room to acclimatize to room temperature.

3.2.3 Computed tomography

The printed cuboids filled with polymer gel were scanned to be able to perform treatment planning delivery. During the scanning set-up it was made sure that the middle of the cuboid's flat surface corresponded to the intersection of the lasers. Scanning was done with the Siemens sensation open in axial orientation: 120 kV, tube current 340 mAs, slice thickness 1 mm and a FOV 512 x 512.

3.2.4 Irradiation, MRI read out

Both cuboids were placed on 20 RW3 plates (figure 3.2). This method ensures full backscatter conditions. MRI read-out is done using an 8-channel head coil using MRI Philips Achieva of 1.5 T. A multi-echo sequence was arranged with a specific slice thickness, 32 equidistant echoes, RT=3000 ms (repetition time), ET=40-1280 ms (echotime), pixel bandwidth of 43 Hz per pixel and a NEX of 1.

Figure 3.2: The set-up: a printed cuboid on 20 water-equivalent RW plates.

The calibration vials were irradiated with their longitudinal axis perpendicular to the applied photon beam. A reference measurement using an ionization chamber indicated the absolute dose given to the vial.

3.2.5 Data processing and calibration

R_2 maps were extracted from 32 equidistant echo images. χ^2 minimization (based on LevenbergMarquardt algorithm) was used to fit these images [54]. A matlab program is used to select manually an ellipsoidal ROI from each calibration vial to calculate the R_2 values and their standard deviation. Subsequently these R_2 values are plotted against their absolute dose. The calibration curve was fitted to a mono-exponential function as explained earlier [11]:

$$R_2 = R_{2,sat} - \Delta R_2 \cdot e^{-\alpha \cdot D} \tag{3.1}$$

3.2.6 Reference measurement

Radiochromic film was chosen to validate the measured dose in the gel. EBT3 film was placed in between water-equivalent plates at the same depth as the acquired slice in the cuboid. This was done while maintaining the same SSD. Figure 3.3 represents the set-up. Calibration of the batch EBT3 was done according to Crijns *et al.* [55]. A γ calculation was performed to evaluate the dose distribution in the gel to the radiochromic film [1].

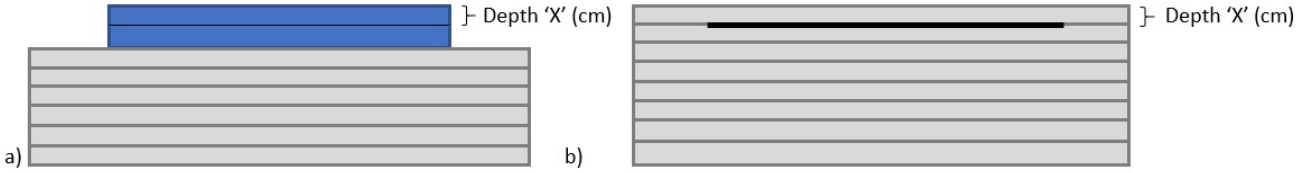

Figure 3.3: Reference EBT3 measurement: a) the cuboid was irradiated onto RW3 plates. The black line represents an MRI slice taken at a specific depth. b) the film is placed in between RW3 plates at the same depth as the acquired slice in the cuboid. Here the thicker black line represents the film.

Chapter 4

A preliminary study

A preliminary study involved the evaluation of the mechanical firmness and determination of the homogeneity and relative electron density. The main goal of this project is to analyse the feasibility of the integration of a 3D gel with dosimetrical properties into a 3D print. To achieve this the 3D printed cuboid must retain it's shape and be watertight.

The dosimetrical part of the preliminary study consisted of 2 printed cuboids each filled with a different batch of polymer gel. The dimensions of cuboid A were 175x175x22.5 mm^3 while cuboid B was 150x150x15 mm^3. They differ in size, batch and applied IMRT fields.

4.1 Materials & methods

4.1.1 Characteristics 3D bolus and gel

Water-tightness was tested by printing little cuboid geometries of 50 x 50 x 10 mm^3. Subsequently holes were drilled in the prints after which these were filled with water.
The printer settings were adapted in such a way that water-tightness of the specific printed cuboid could be guaranteed. The FELIXbuilder manual was used to analyse the different settings.

Mechanical firmness tests and evaluation of the characteristics of the bolus involved a printed cuboid of 150 x 150 x 10 mm^3. These cuboids were filled with gelatine, the non reactive component of the polymer gel.
An axial helical CT scan was taken with the Siemens sensation open. The used parameters are an energy of 120 kV, a slice thickness of 1 mm, FOV of 512 x 512 and a tube current of 340 mAs. In addition the program MIM was used was used to extract a number of metrics from the CT images.

4.1.2 Polymer gel dosimetry

The entire process of obtaining a dosimetric signal from the gel was specified in section 3.2. The next few paragraphs will focus on the specific treatment delivery parameters and the set-up used to deliver the dose to the calibration vials and cuboids.

Treatment delivery IMRT

Cuboid A Cuboid A involved an existing lung IMRT field (12.5 x 12.8 cm^2) using the sliding IMRT technique. The technique involved the Truebeam linac, a 6 MV beam with a static gantry at 0°, a dose rate of 600 MU/min and an SSD of 100 cm. The chosen field was applied 9 times with 218 MU per field. This was done to ensure that a high dose was absorbed in the phantom.

Cuboid B Another existing lung IMRT field (9.7 x 12.6 cm^2, sliding technique) was selected for cuboid B with a static gantry at 0°. A dose rate of 600 MU/min was applied at an SSD of 90 cm. The field was delivered 10 times and each field contained 181 MU.

Irradiation set-up

The calibration tubes were inserted in the farmer chamber insert which was located in one of the RW3 plates and placed on the ground in between several other RW3 plates (SSD 2m). This way the calibration vials were irradiated perpendicular to their longitudinal axis. Unfortunately the tubes couldn't be inserted to the point where the reference measurement with a Farmer type (FC65G) ionization chamber was done. The distance between FC and the calibration vials was about 10 cm. The parameters were: 1018.7 hPa, a temperature of 22.0°C and 1.0002 Gy corresponded to 457 MU.

Reference measurement

Subsequently radiochromic films (EBT3) were placed at 0.75 cm depth for cuboid A and 0.5 cm for cuboid B. These depths were obtained using the RW3 water equivalent slabs with different thicknesses.

MRI read-out & data processing

Each cuboid was scanned separately with a styrofoam construction as in figure 4.1. The slices, of 5 mm thick, were taken as presented in figure 3.3.

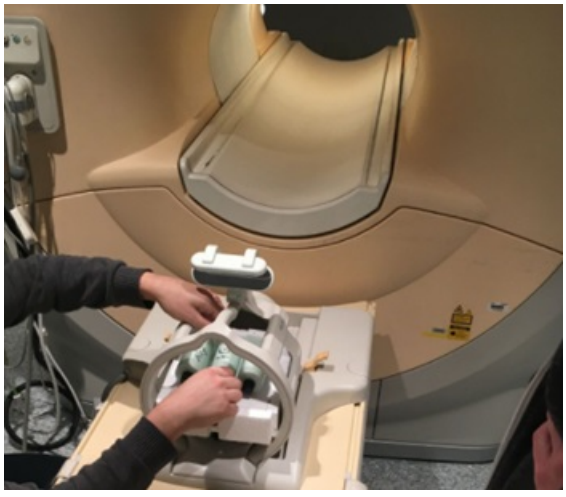

Figure 4.1: Read-out set-up for cuboid A and B: prints and calibration vials were surrounded by a styrofoam construction and put in a 8-channel head coil.

Cuboid A The MRI slice was taken along the longitudinal axes of the cuboid and calibration vials. The ellipsoidal ROI for each calibration vial was demarcated as in figure 4.2.

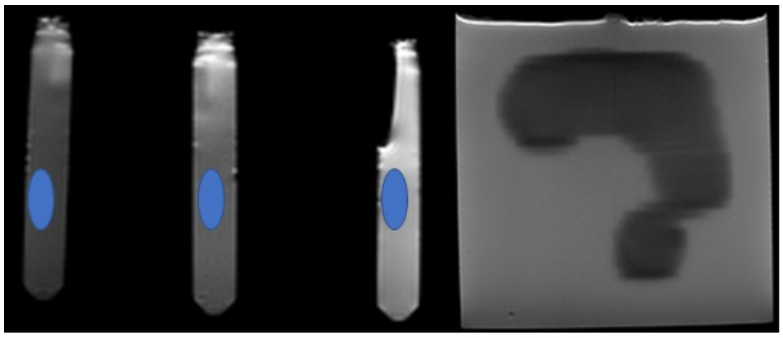

Figure 4.2: Acquired MRI images corresponding to cuboid A. Left: calibration vials, right: slice at approximately 0.75 cm depth in cuboid A.

Cuboid B The same procedure was applied for cuboid B. Figure 4.3 illustrates the selected MRI images.

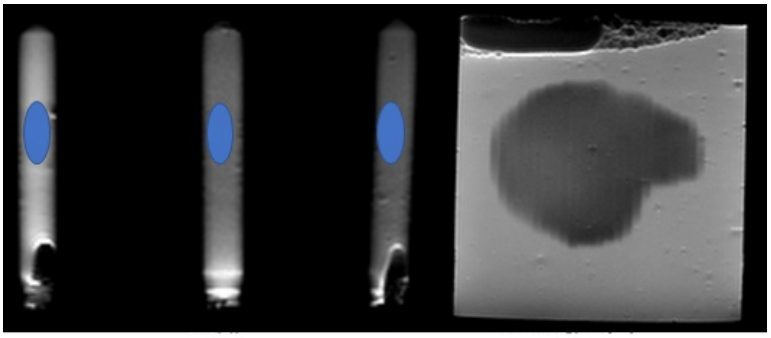

Figure 4.3: Acquired MRI images corresponding to cuboid B. Left: calibration vials, right: slice at approximately 0.5 cm depth in cuboid B.

4.2 Results

4.2.1 Characteristics 3D bolus and gel

Water-tightness

Figure 4.4 illustrates the geometry of the cuboids which were tested for watertightness. Figure 4.4 represents the printed cuboids (A till H). Parameters of print A were default settings included in the program 'Felixbuilder'. Table 4.1 specifies the used parameters. Important changes in comparison to the previous cuboid are highlighted in blue.

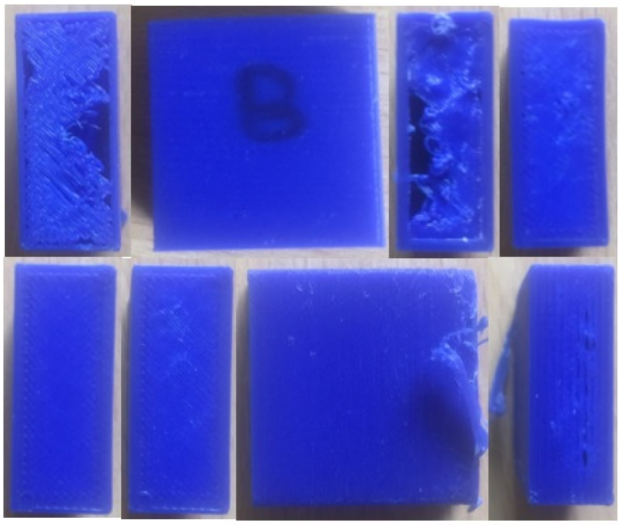

Figure 4.4: First row left to right: Cuboid A till D, second row left to right: E, F and two sides of G. In blue: changes in comparison to the previous cuboid.

Cuboid A resulted in too much infill and an unattached roof. The next print appealed to be a firm structure. However when pressure was applied the roof, bottom and walls started to leak. The upskin of cuboid C also failed to attach to the contours. This problem was solved in cuboid D but water was still leaking from the roof. Cuboid E was confirmed as the first watertight print. Hoping to reduce the number of layers cuboid F was printed. Unfortunately the watertight test failed. At last cuboid G was printed on a small ramp to see if the results could be improved. The roof couldn't attach properly to the surrounding contours and thus also failed. The different selected settings can be found in table 4.1.

Table 4.1: Available printer settins.

	A	B	C	D	E	F	G
Contours	vlak	vlak	vlak	vlak	vlak	vlak	10°helling
Number of contours	2	3	4	4	4	4	4
Contour overlap	0,5 mm	0,6 mm	0,6 mm	0,6 mm	0,6 mm	0,6 mm	0,6 mm
Contour	Before Infill	Before Infill	Before Infill	Before Infill	Before Infill	Before Infill	Before Infill
Offset	100% of Default	100% of Default	75%	75%	75%	75%	75%
Hatching order	InnerContourFirst	InnerContourFirst	InnerContourFirst	InnerContourFirst	InnerContourFirst	InnerContourFirst	InnerContourFirst
Print speed factor	50%	30	30%	30%	30%	30%	30%
Extrusion factor	85%	85	85%	85%	85%	85%	85%
Thin walls							
Enabled	yes	No	No	No	No	No	No
double the walls	yes	No	No	No	No	No	No
start point relocation							
Mode	SharpestAngle	Random	Random	Random	Random	Random	Random
Upskin							
Number of layers	3	4	5	5	5	4	4
Line distance	90% of Default	100% of Default	50%	95%	95%	95%	95%
Infill overlap	0	30%	0%	0%	75%	80%	75%
Angle	45°	45°	45°	45°	45°	45°	45°
Angle increment	90°	90°	90°	90°	90°	90°	90°
Print speed factor	60%	40%	40%	40%	40%	40%	40%
Extrusion factor	85%	85%	85%	85%	85%	85%	85%
Downskin							
Number of layers	3	4	5	5	5	4	4
Line distance	90% of Default	100% of Default	50%	95%	95%	95%	95%
Infill overlap	0%	30%	0%	0%	75%	80%	75%
Angle	45°	45°	45°	45°	45°	45°	45°
Angle increment	90°	90°	90°	90°	90°	90°	90°
Print speed factor	60%	40%	40%	40%	40%	40%	40%
Extrusion factor	87.50%	87.50%	87.50%	87.50%	87.50%	87.50%	87.50%

Mechanical firmness

Cuboids were created with dimensions of 150 x 150 x 10 mm^3 to perform these tests. The prints were filled with the non-dosimetric component of the gel. It was immediately clear that the contours of the print were not firm enough to withstand the pressure of the gelatine which was poured at 32°C in the cuboid.
The fact that the gelatine is more dense than water resulted in a disintegration of the sides from the cuboid: a convex form was observed (figure 4.5). More contour layers were printed as a countermeasure, this resulted in a firm cuboid.

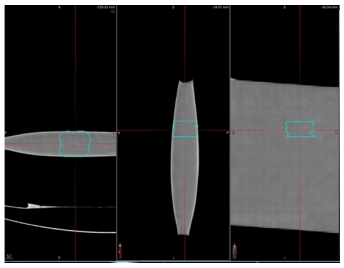

Figure 4.5: CT scan of a cuboid (150 x 150 x 10 mm^3) filled with gelatine. Left to right: top view, side view and front view.

Homogeneity and electron density

A necessary property of a bolus is its homogeneity. This way each part of the bolus will build-up the dose equally. Hence an analysis in the program 'MIM' was performed on CT scans to check the homogeneity of the gelatine.
Figure 4.6 displays the thick walled cuboid printed at 175°C. The pink contours include the selected part of the gelatine for statistical analysis. Figure 4.6 indicates that the gelatine HU values of the gelatine are relatively gaussian distributed. A mean value HU of 36.46; a median of 34 and a standard deviation of 10.99 were observed. The right tail of the histogram is a result of the transition between the gelatine and the wall which cannot be seperated clearly in a CT scan. A potential cause could be the partial volume effect.
This however does not prove the homogeneity of the gelatine. Eventually some regions can be more dense than others. Therefore matlab was used to create histograms and profile lines.

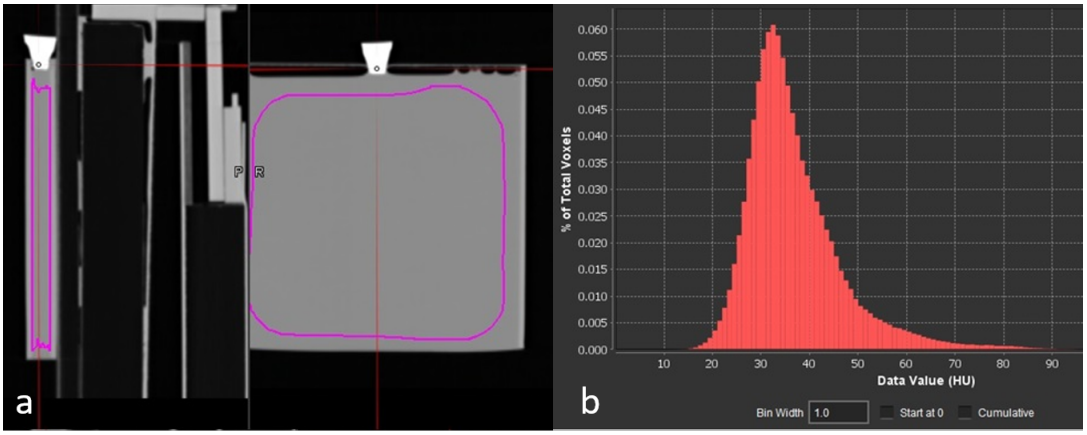

Figure 4.6: (a)CT scan of a cuboid (150 x 150 x 10 mm^3) filled with gelatine. Contours in pink represent the selected part of the gelatine for analysis.(b)Histogram of the HU from the gelatine.

The bolus was divided in 6 equal parts as illustrated in figure 4.8. Histograms of these parts are presented in figure 4.7. It is clearly visible that the shape of each histogram is quite similar for each section of the cuboid.

The biggest group of pixels is found in the intensity region of 1040 (21.4 HU) till 1070 (51.0 HU) which corresponds to the value of gelatine. Table 4.2 specifies the mean and median values. The calculated HU values correspond to the ones presented in MIM.
Another test involved visualising the pixel intensities in function of the distance, which is perpendicular to the flat surface of the cuboid (figure 4.9). The profiles were selected randomly throughout the print in regions 1 till 6 (figure 4.8). The statistical noise of the CT scanner was $\pm$ 10 HU (1HU $\approx$ 1 value of pixel intensity). An average pixel intensity of 1062 was observed for the gelatine, making the outer boundaries 1052 and 1072. The observed higher intensities on both sides of figure 4.9 represent the PLA shell of the cuboid.

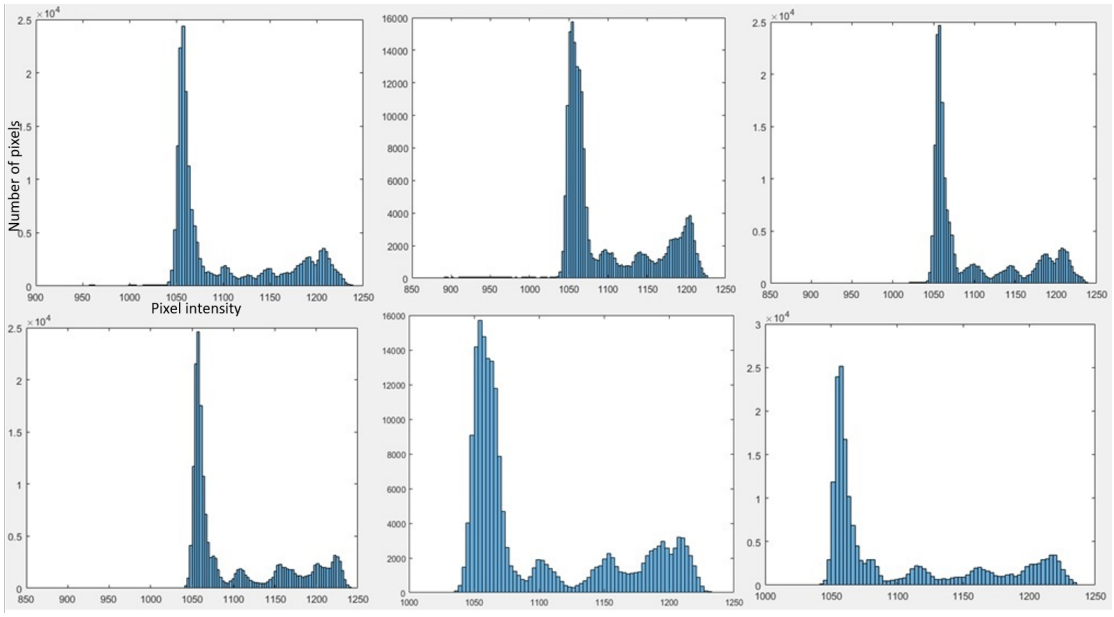

Figure 4.7: Corresponding histograms. First row left to right: 1 till 3, second row: 4 till 6. Axes on the other figures are omitted.

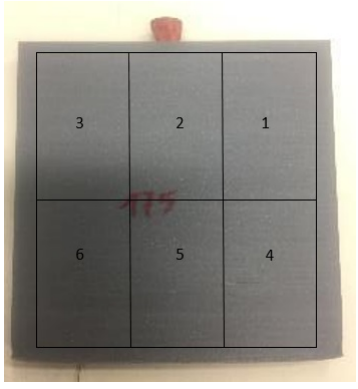

Figure 4.8: Illustration of the division of the printed structure. The left side of the cuboid is darker due to a shadow which was incident upon it.

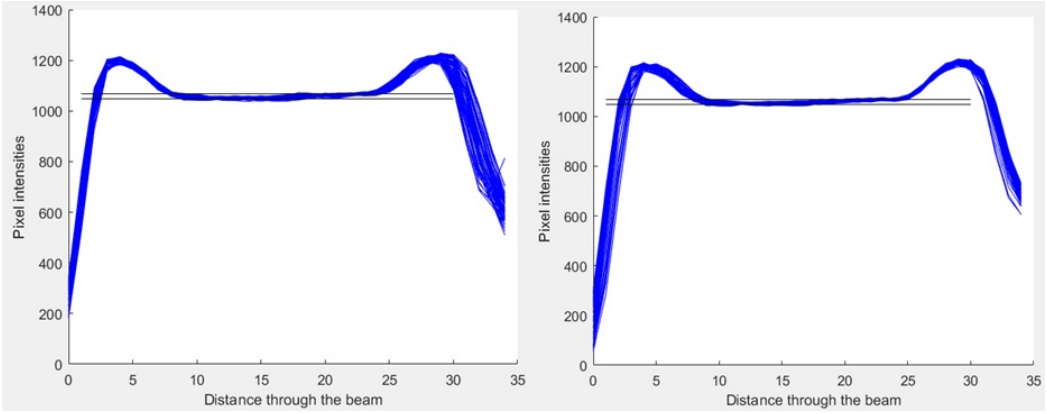

Figure 4.9: Profiles taken perpendicular to the flat surface of the beam at arbitrary spots. Statistical noise is presented as black lines for the gelatine component (± 10 HU, 1 HU ≈ 10 pixel intensity).

Table 4.2: Pixel intensity median, average and HU value of the parts in figure 4.8.

1	Intensity pixel	HU	2	Intensity pixel	HU	3	Intensity pixel	HU
Median	1064	45		1066	47		1065	46
Average	1100	80		1097	77		1100	81
4	Intensiteit pixel	HU	5	Intensiteit pixel	HU	6	Intensiteit pixel	HU
Median	1065	46		1066	47		1066	47
Average	1100	81		1100	80		1103	84

No air gaps were observed during these experiments. This is reflected in the displayed histograms: no intensity value near 0 was observed.

Electron densities can be calculated from the measured HU's. Results were obtained using simple interpolation between known calibration phantoms in the HU calibration curve of the CT scanner. Table 4.3 reports the electron densities with corresponding HU values.

Table 4.3: Electron densities with corresponding HU values.

Measured HU	45-47	155-190
$\rho_{e,water}$	1.038-1.040	1.103-1.126
Mass density	1.057-1.059	1.132-1.159

4.2.2 Polymer gel dosimetry

In this preliminary study 2 cuboids were printed and each filled with a different batch of the gel. Each cuboid was scanned with 3 calibration vials. Cuboid A had dimensions of 175x175x22.5 mm^3 while cuboid B measured 150x150x15 mm^3. One MRI slice of 5 mm thick was obtained for each cuboid. Both were compared to the calculated dose distribution from the exported dose plane (TPS) and radiochromic film (EBT3).

Cuboid A

The fitting of the R_2 values to their absolute dose was done by using a mono-exponential function:

$$f(x) = a \cdot e^{-b \cdot x} + c$$

The calibration tubes with 1, 4 and 12 Gy measured an R_2 [s^{-1}] 1.32 ($\pm$0.0039) , 2.06 ($\pm$0.008) and 2.76 ($\pm$0.00092). The fitting parameters stated a=-1.97, b=0.21, c=2.93 and R^2 of 1. Figures 4.10 displays the results.

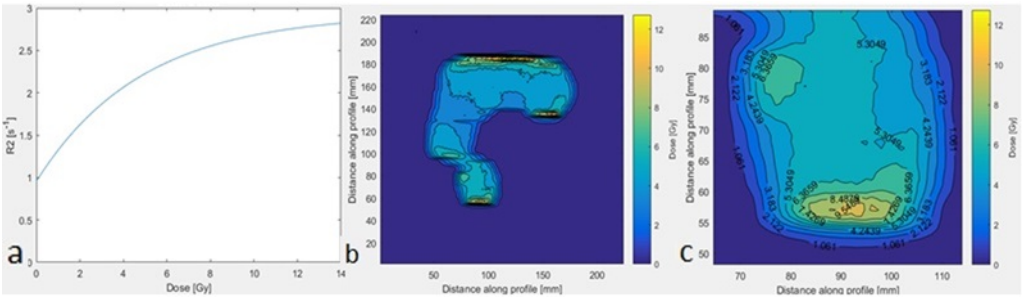

Figure 4.10: Cuboid A: a) calibration curve b) converted R_2 map to dose c) enlarged part of the dose map with isodose contours.

Subsequently dose planes were exported from the TPS to be compared to the gel. The absence of markers on the print made it very difficult to find a plane in the TPS which corresponds to the measured dose. An exported plane at 0.72 cm depth resulted in 93.04% (3%/3 mm). A mean gamma of 0.45 $\pm$0.33 with a mean dose difference and standard deviation of 0.99 $\pm$13.85 [%] was observed. Visualising of the measured and calculated variables can be seen in figure 4.11.

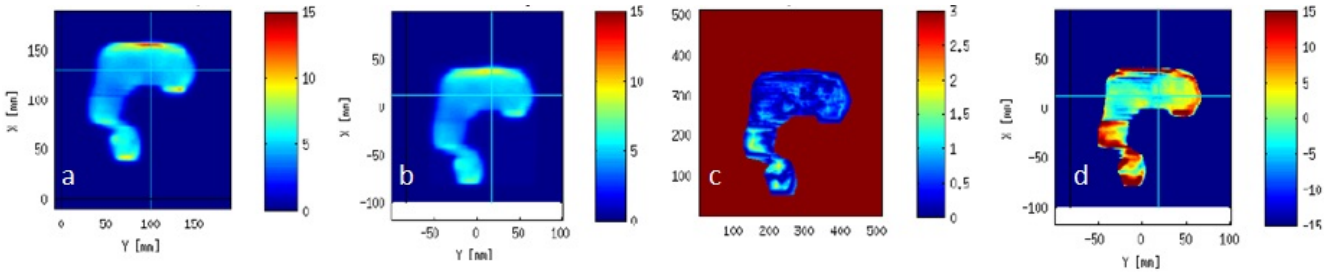

Figure 4.11: Cuboid A: a) measured dose distribution in the gel [Gy], b) calculated dose distribution (TPS) [Gy], c) gamma map evaluation and d) the dose difference [%].

Cuboid B

The same routine was applied to cuboid B. For 1, 6 and 12 Gy $R_2(s^{-1})$ values of 1.30 ($\pm$0.0043), 2.32 ($\pm$0.0106) and 2.72 ($\pm$0.0105) were observed. Corresponding fitting parameters are a=-1.95, b=0.20 and c=2.89 with an R^2 of 1. Figure 4.12 represents the calibration curve and the measured dose map coming from the phantom.

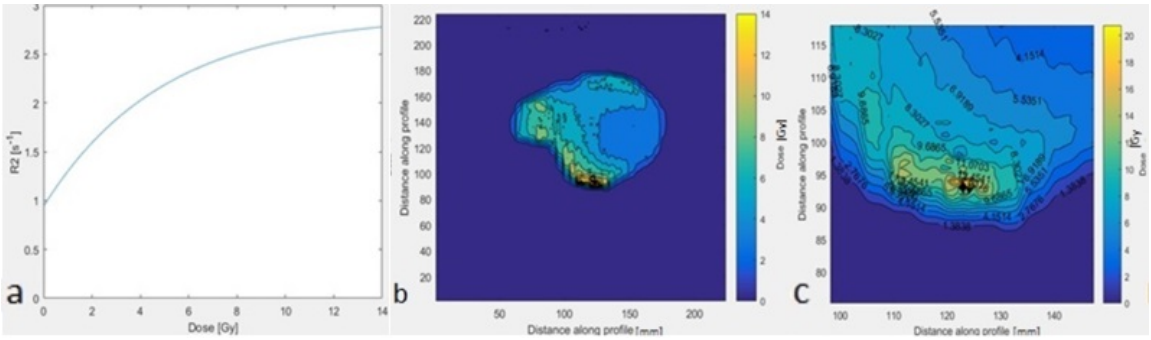

Figure 4.12: Cuboid B: a) calibration curve b) converted R_2 map to dose c) enlarged part of the dose map with isodose contours.

A surface was taken in the TPS to be compared to the gel. The problem of absent markers was also present here. The MRI localizer estimated the slice was taken at a depth of approximately 0.50 cm. Eventually an exported dose plane at 0.30 cm depth from the surface of the phantom resulted in a 73.31% gamma (3%/3 mm) agreement score. Figure 4.13 displays the distributions of the most important variables.

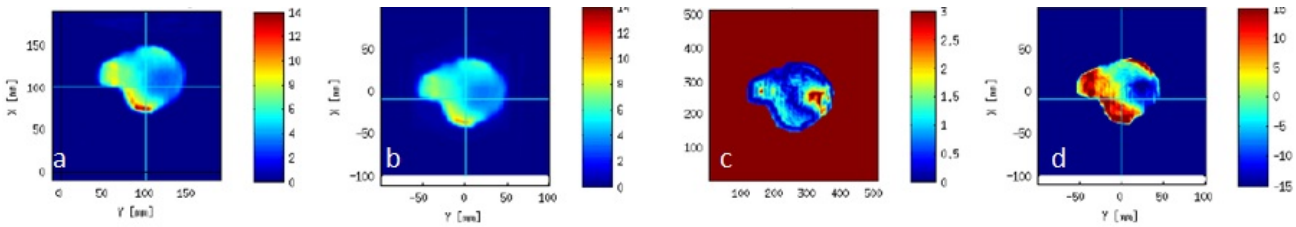

Figure 4.13: Cuboid B: a) measured dose distribution gel [Gy], b) calculated dose distribution (TPS) [Gy], c) gamma map evaluation and d) the dose difference [%].

Film dosimetry verification

Cuboid A A piece of EBT3 film was placed at a reference depth of 0.75 cm in between water equivalent RW3 plates. The results included: 80.66% (3%/3 mm), mean γ value and SD 0.60 $\pm$0.50 and mean dose difference with SD [%] 3.89% $\pm$8.13.

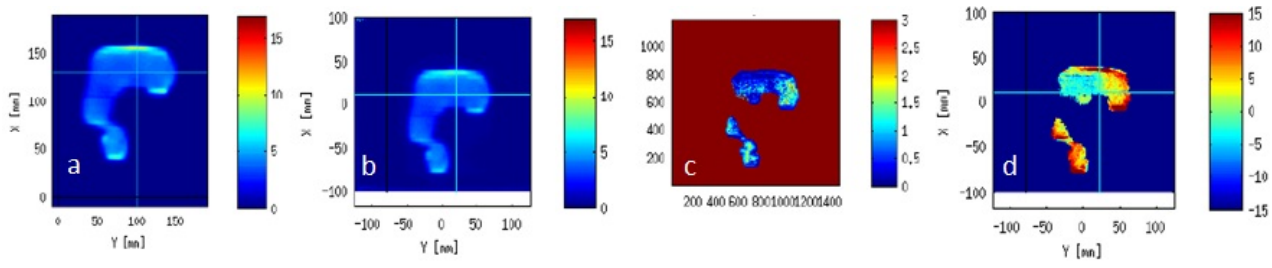

Figure 4.14: Cuboid A: a) distribution in the gel [Gy], b) film dose distribution [Gy], c) gamma map evaluation and d) the dose difference [%].

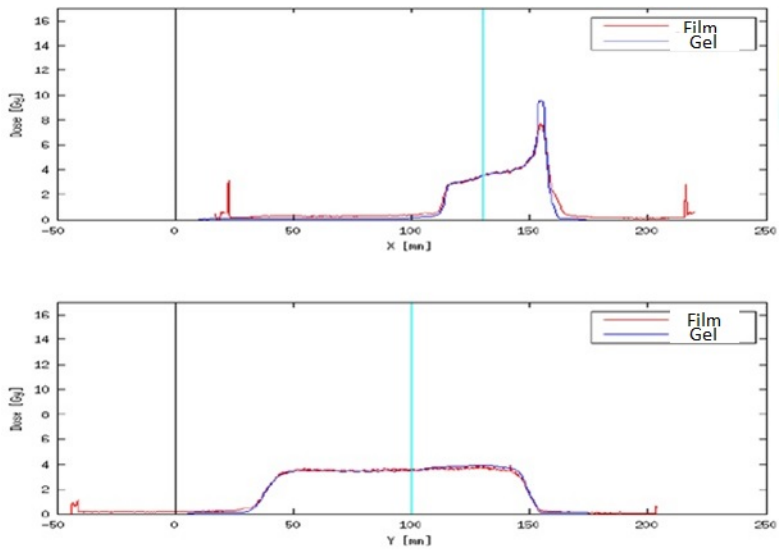

Figure 4.15: Cuboid A: dose profiles in the X and Y direction along the light blue lines presented in figure 4.14.

Cuboid B A score of 39.20% (3%/3 mm) was obtained by comparing the film at 0.50 cm depth using RW3 water equivalent plates. A mean γ score of 2.01 $\pm$ 1.84 was calculated (Figures 4.16 and 4.17). An evaluation between the exported dose plane at 0.50 cm from the TPS and film at 0.50 cm was assessed due to the previous score. A gamma 3%/3 mm revealed only 46.26% matching values within the criteria.

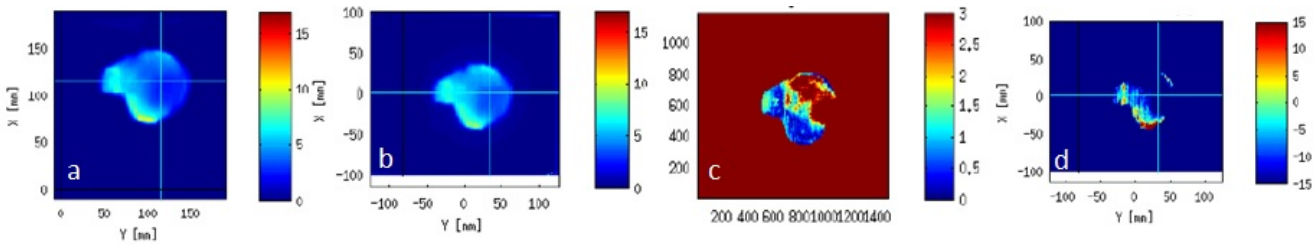

Figure 4.16: Batch 1: a) distribution in the gel [Gy], b) film dose distribution [Gy], c) gamma map evaluation and d) the dose difference [%].

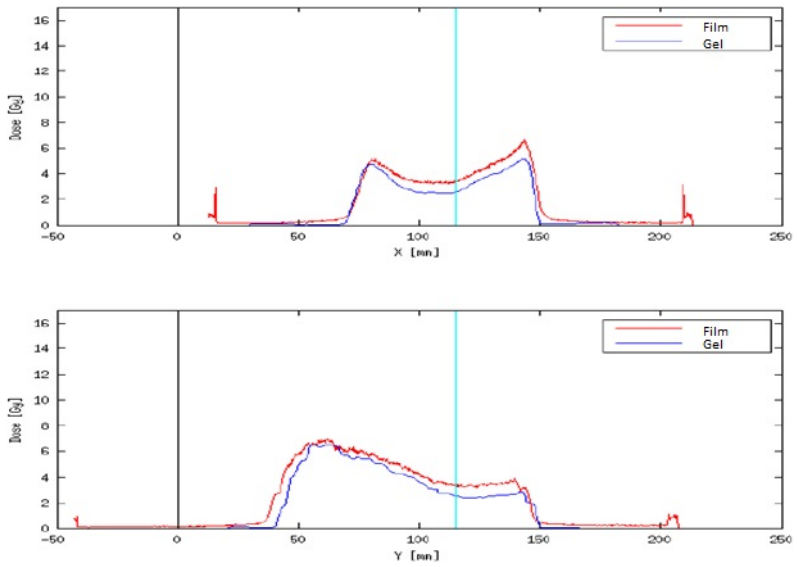

Figure 4.17: Batch 1: dose profiles in the X and Y direction along the light blue lines presented in figure 4.16.

4.3 Discussion

4.3.1 Characteristics 3D bolus and gel

A necessary property of a watertight print is a satisfactory number of layers in the contours, upskin and downskin. Care must be taken when specifying the line distance in the upskin and downskin. If not, the printer will repeatedly pull the previous printed line off the roof when the distance between the lines is set too short. The printing of the roof improves significantly when an overlap is set with the inner contour. The temperature at which the cuboid is printed also plays a role in the result. It was observed that a temperature of 195°C was optimal in the case of the PLA filament.

The homogeneity of the print is consistent in each evaluated part of the filled print. Figure 4.9 shows that the gelatine is homogeneous and within the statistical noise which is ± 10 HU. The right tale of the graph shows some differences. This is because the profiles were taken perpendicular to the cuboid and at the end, the PLA shell merges with the couch (partial volume effect [56]).

Small regions of intermediate intensities between the two main peaks are due to the partial volume effect (PVE). This effect becomes more visible when looking at small regions of interest, for example the region between the printed shell and the gelatine. Because of this there are arrays of pixels which have overlapping materials. These show a mixture of materials due to the finite resolution of the imaging technique [57].

The displayed relative electron density values are only intended to give an indication of the water-equivalence. As can be derived from table 4.3 the $\rho_{e,water}$ of gelatine is nearly equal to that of solid water. The printed PLA shell which has a thickness of 3-4 mm has a slightly greater density and should be taken into consideration.

4.3.2 Polymer gel dosimetry

Cuboid A Cuboid A received rather good scores with the corresponding TPS slice at 0.72 cm (93.04%). However due to circumstances the exact depth of the acquired slice was not known. A lot of TPS planes were exported and evaluated to the distribution in the gel before this result was obtained.

It should be emphasized that the slice thickness of the MR slice was 5 mm. And thus the dose will be averaged along 5 mm depth in the gel. It is rather difficult to obtain conclusive evidence when comparing to the TPS or film dose distribution because both have a thickness in the order of 10^{-2} mm. In combination with the uncertainty of the position of the slice, care should be taken in the interpretation of these results.

The acquired slice was measured in the build-up of the beam. In this region, the dose gradient is very steep which means a small variation in depth results in a large change in dose.

When comparing the calibration curve in section 4.2.2 to the ones in the literature it is apparent that the obtained curve is not quite as linear. Also much higher R_2 values were registered. A possible explanation may be the heating of the gelatine, which at a specific temperature forms shorter chains and becomes less mobile.
An independent measurement of the dose was done using an ionisation chamber in the middle of the irradiation field. The calibration vials were too large to be able to fit all the way in the insert made for the FC65G and were placed at a distance of approximately 10 cm from the point of measurement. This was largely compensated by increasing the distance between the source and the vials to its maximum. Nevertheless, it should be kept in mind that this could contribute to the resulting dose deviation between measured and calculated dose distribution. Also, only 3 calibration vials were accessible to perform the calibration.

When looking at figure 4.11 it is clear that large overshoots are observed. This could be partly attributed to the MRI read-out set-up. Styrofoam was used to insulate both calibration vials and the cuboid. It could be that due to the power dissipation of the MRI an offset in temperature between the cuboid and calibration vials was introduced. Vandecasteele and De Deene observed during their experiments in 'On the validity of 3D polymer gel dosimetry: III. MRI-related error sources' that an offset of 1°C at a temperature of 20 °C dose overestimations of 8.6% can occur. This phenomenon becomes more pronounced as the offset between both increases [40]. Figure 2.11 in the section dose error factors illustrates this.

Cuboid B All of the uncertainties from cuboid A also apply to B because both underwent the irradiation and read-out equally. An agreement score at 0.3 cm depth in the TPS resulted in 73.31%. A region of underdosage and a region of overdosage can be seen in figure 4.13. This indicates to oxygen exposure. Slices taken near the PLA shell have an increased chance of being exposed to oxygen. Depending on its concentration, this could have a promoting or inhibiting effect. High concentrations could dehydrate the gel resulting in large R_2 values and thus overestimations. Low concentrations inhibit the polymerization process resulting in an underdosage [42].

Also in this cuboid some regions of the irradiated field show large peaks. This phenomenon seems to be more pronounced (for cuboid A as well as B) near the edge of the field where steep dose gradients are apparent(figure 4.18). The literature states that the time between irradiation and read-out must be long enough to let the gel stabilize. A written report from De Deene *et al.* explains that only after 12 hours post-irradiation the peaks started to decrease [44]. The produced gel in our research only had 11-12 hours between the two.

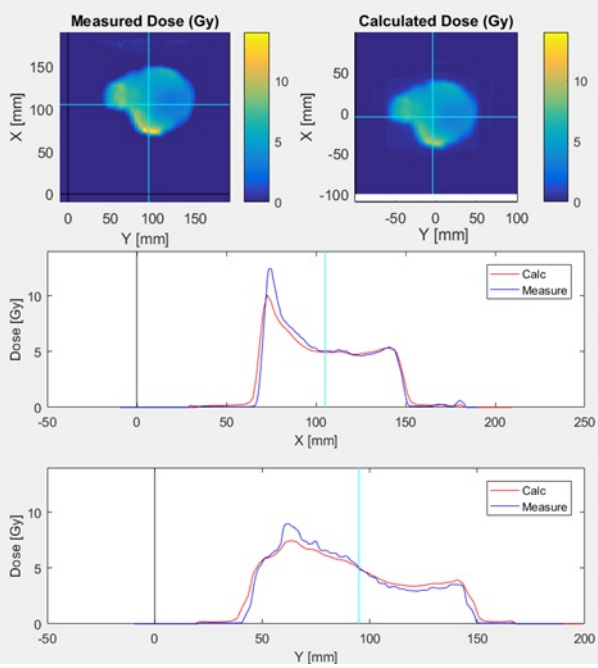

Figure 4.18: Comparison between the measured dose distribution of the gel to the calculated distribution from the TPS. Profiles along the blue lines of the X and Y axis are also displayed.

Another factor could be some artefacts from the B_0 map. However only a variation of ± 20 Hz was observed at the boundaries of the scan. This results in 0.31 ppm variance which is negligible.

Film dosimetry verification

Cuboid A A result of 80.66% was obtained between the gel and film placed at 0.75 cm. Figure 4.15 shows a pronounced region in the irradiated field where the gel exhibits less dose than the film. This could indicate that the acquired slice from the gel was located a bit further in the build-up zone.

Cuboid B Cuboid B only scored 39.20% on the 3%/3 mm criteria at 0.50 cm depth. Figure 4.16 illustrates regions where a lower dose is measured in the gel. Dose profiles drawn in figure 4.17 also indicate that the acquired slice was probably situated more in the build-up region. Namely, the edges of the irradiated field don't align properly. The gel data possesses a smaller width than the film. This supports the hypothesis because the beam of the linac diverges with increasing depth.

4.4 Conclusion

This preliminary study illustrated the homogeneity of the used gel. Also, a lot of uncertainties were introduced in this study: the irradiation of the calibration vials, the thickness of the slice combined with a measurement in the build-up zone and the uncertainty of the slice position in both cuboids.
Large dose overshoots could be due to the fact that the gel didn't have enough time to stabilize in between irradiation and MRI read-out. An important factor may also be the offset in temperature between calibration vials and the cuboids.

Chapter 5

Second run

A second run occupied two printed cuboids with dimensions 175x175x30 mm^3 from the same batch of polymer gel. Cuboid A received the same IMRT field as cuboid A from the preliminary study while B received the same one as B. The procedure of obtaining a dosimetric signal from the gel has already been described in section 3.2. Because of the introduced uncertainties in the preliminary study, some adaptations were made in the irradiation set-up and MRI read-out. Care was also taken during slice selection, to reduce the uncertainty in position.

5.1 Materials & methods

5.1.1 Set-up of the second run

Treatment delivery

The calculated plans in the TPS from the first run were copied onto the two cuboids of the second run. Plan A was copied onto A and B onto B. A difference was the SSD which was set for both cuboids at 90 cm.

Irradiation set-up

Due to dose uncertainties related to the set-up of the irradiation of the calibration vials during the first run a different set-up was considered. A handmaid construction involved the positioning of a calibration vial in a water tank (1D scanner [58]) at a depth of approximately 10-12 cm. The water tank was placed at the middle of the beam and had an SSD of 90 cm. The longitudinal axes of the vials were placed perpendicular to the applied beam. The farmer chamber (FC65G) was put at the same depth a few centimetres next to the vial. A homogeneous field of 20 x 20 cm^2 was applied. The advantage of this set-up was the fact that the ionization chamber could continue to assess the dose delivered to each vial and no air gaps were introduced. Figures 5.1 and 5.2 show the experimental set-up. Atmospheric conditions were: 999 hPa, 22.4 °C and 0.9999 Gy corresponded to 112.2 MUs.

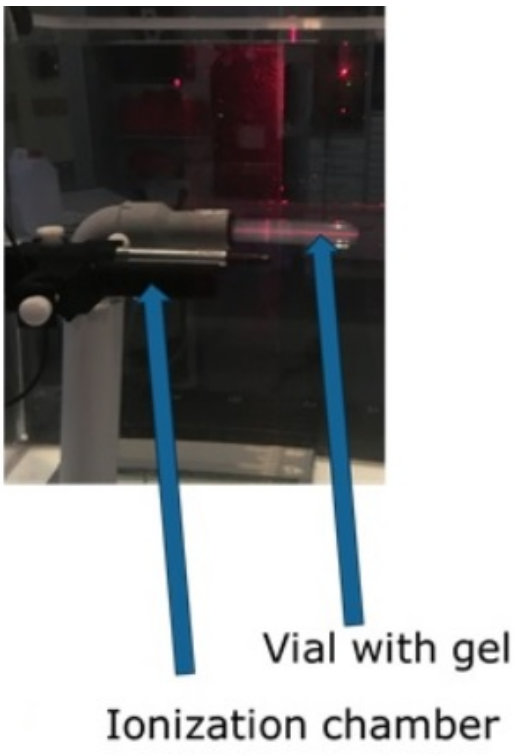

Figure 5.1: Irradiation of the calibration vials from the second run in a water tank.

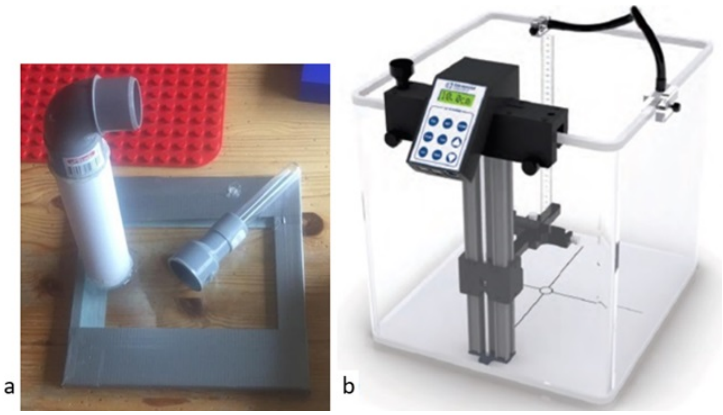

Figure 5.2: a) The fabricated construction which was placed in the 1D scanner water tank. b) The used 1D scanner water tank [58].

MRI read-out

The construction for MRI-read out consisted of a plastic water tank filled with contrast liquid. It was made sure that the inserted cuboid was completely under water, doped with a contrast liquid. The set-up included the possibility to insert 5 calibration tubes next to the cuboid to be scanned. Figure 5.3 illustrates the set-up visually. Here a slice thickness of 2 mm was assessed. Additionally a change in RT value was made: 8000 ms. Both cuboids with each 5 calibratoin vials were scanned. A third scan involving all the calibration tubes was attained (figure 5.4). 10 slices of 2 mm were taken for both cuboids (2 cm of gel layers were available in each cuboid) and 5 were acquired for the third scan involving all the test tubes.

Figure 5.3: Read-out set-up for run 2: each cuboid was placed onto the support structures and completely surrounded by water doped with contrast liquid. The calibration vials were inserted next to the cuboid in the provided holders. Eventually the construction was placed in a 8-channel head coil which would be inserted in the MRI imager.

Figure 5.4: Scanning set-up for the calibration vials. The water tank was also placed in a 8-channel head coil.

To summarize three different scans were made during the second run: cuboid A, B with each 5 (figure 5.3) calibration vials (1,2,3,8 and 12 Gy) and a third scan involving 14 irradiation tubes (5.4).

Data processing

Cuboid A The current scanning set-up made sure cuboids and vials could be scanned together in one slice. Circular regions of interest were submitted as illustrated in figure 5.5.

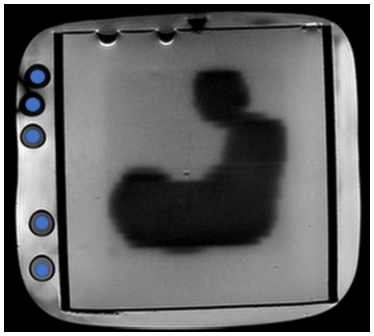

Figure 5.5: Echo of a MRI slice from cuboid A. ROI for acquisition of the mean R_2 and standard deviation are coloured in blue.

Cuboid B Cuboid B exhibited a similar set-up (figure 5.6).

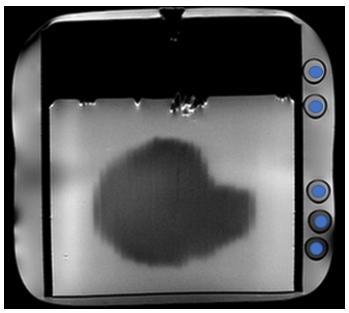

Figure 5.6: Echo of a MRI slice from cuboid B. ROI for acquisition of the mean R_2 and standard deviation are coloured in blue.

Reference measurement with radiochromic film

EBT3 films were placed at 10 mm and 20 mm depth for both fields using the same method as described in section 3.2. The thickness of the PLA shell (0.5 cm) has a greater relative electron density than the RW3 plates. To account for this the mean dose value of 2 adjacent slices was obtained. Table 5.1 shows the slices used to average the dose.

Table 5.1: A representation of the corresponding slices to the depth at which the EBT3 film was placed.

EBT3 depth [cm]	Slice number	Depth slice [cm]	Resulting depth [cm]
	2	0,7-0,9	
1	3	0,9-1,1	0,9
	7	1,7-1,9	
2	8	1,9-2,1	1,9

5.1.2 Second run: intra-scan study

In this study the variation in calibration fitting parameters between slices at different depths from the same scan is addressed. Figure 5.11 shows the division of the gel into 10 slices. For cuboid A: in the previous study the selected ROIs for calibration came from slice 6. The intra-scan study for cuboid A involved the selection of ROIs for calibration in slice 5 (less deep).
For cuboid B: the selected ROIs to obtain the calibration fitting parameters came from slice 7. The intra-scan study for cuboid B involved the fitting parameters from slice 5 which was less deep.

5.1.3 Second run: inter-scan study

In this section the calibration parameters for cuboid A and B from the second run were switched. Thus cuboid A was calibrated with the parameters of B and subsequently B with the parameters of A. Figure 5.7 shows the principle.

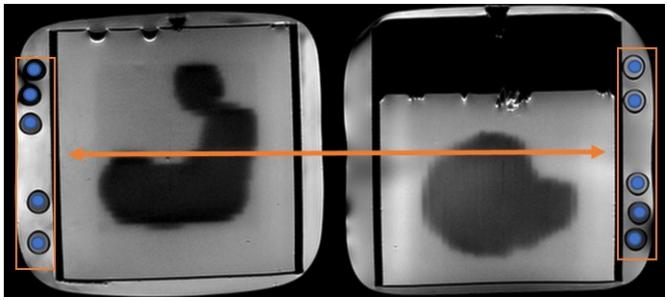

Figure 5.7: Left: cuboid A, right cuboid B. The fitting parameters coming from the ROIs were interchanged to assess the inter-scan study.

5.1.4 Second run: inter-scan study using third scan with calibration vials

In this section 14 calibration vials from the third scan were used to make a calibration function. This function was then applied to cuboid A and B in the hope to attain a more accurate dose distribution. Figure 5.8 shows an echo slice of the third scan.

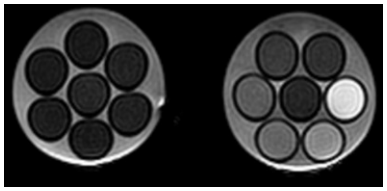

Figure 5.8: 14 calibration vials scanned in a third scan. Doses: 0,1,2,3,5,6,8,9,10,11,12,13,14 and 15 Gy.

5.2 Results

5.2.1 Second run

The second run included two printed cuboids of 175x175x30 mm^3 filled with polymer gel from the same batch. The printed wall of both cuboids had a thickness of 0.5 cm resulting in 2 cm layers of gel. The same 5 calibration vials used during the MRI read-out of cuboid A were also used during the scanning of cuboid B.

Cuboid A Originally 5 calibration tubes had to be assessed for cuboid A. However a MRI artefact was situated in the fourth vial (8 Gy) which resulted in an abnormal high R_2 value and thus could not be used to fit the calibration curve. The arrow in figure 5.9 shows the artefact which was presented in all slices from cuboid A.

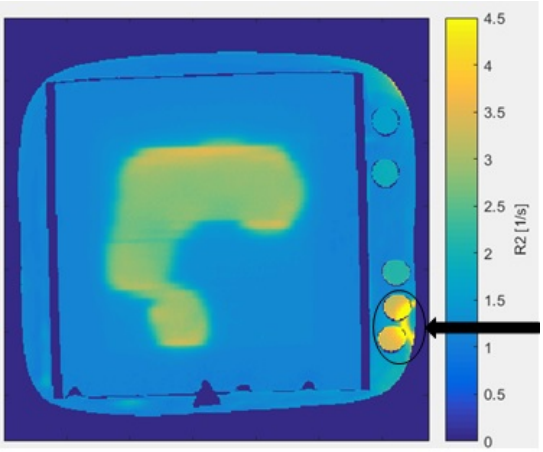

Figure 5.9: An R_2 map of cuboid A: the black arrow indicates the artefact. Due to this higher R_2 values are measured when a ROI is selected.

As a consequence of this only 4 calibration tubes were considered at 1,2,3 and 12 Gy. Parameters a, b and c are defined as -2.964, 0.1117 and 4.27. The goodness of the fit showed an adjusted R^2 of 0.9999. Figure 5.10 shows the fitted curve through the experimental data. Slice 6 (figure 5.11) was chosen to select the ROIs because it was well situated in the water. This was done to minimize the temperature offset between the selected ROI and the cuboid.

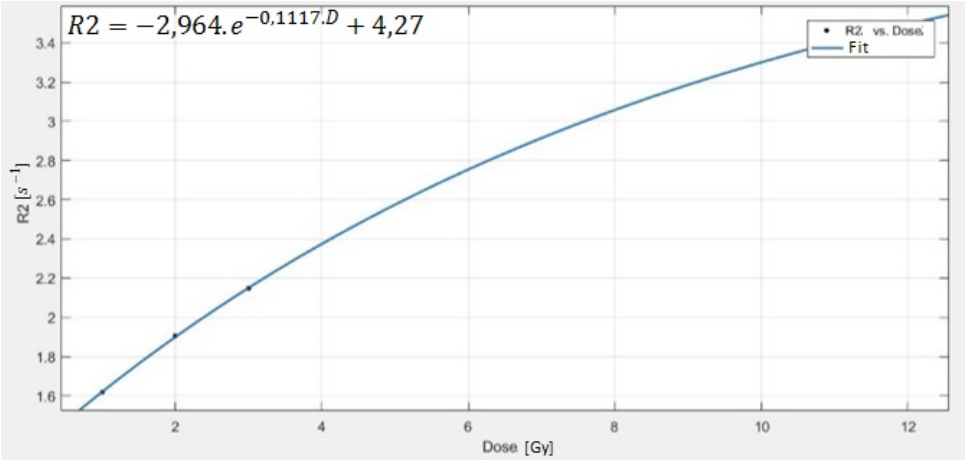

Figure 5.10: Calibration curve linked to cuboid A using the 4 calibration vials (8 Gy is omitted). The R_2 value is plotted as a function of the dose.

Comparison to calculated TPS dose planes A total of 10 slices were acquired during the scanning of cuboid A from which 8 were found useful to be compared to the exported dose planes. The TPS exported dose planes were always situated in the middle of slice of gel. Figure 5.11 displays the principle. The shell was 0.5 cm thick while each slice of gel was 0.2 cm thick. TPS planes were exported thus at depths of 0.8 cm till 2.2 cm with a constant interval of 0.2 cm in between. Figure 5.12 represents an example of dose profiles in slice 3 of the cuboid.

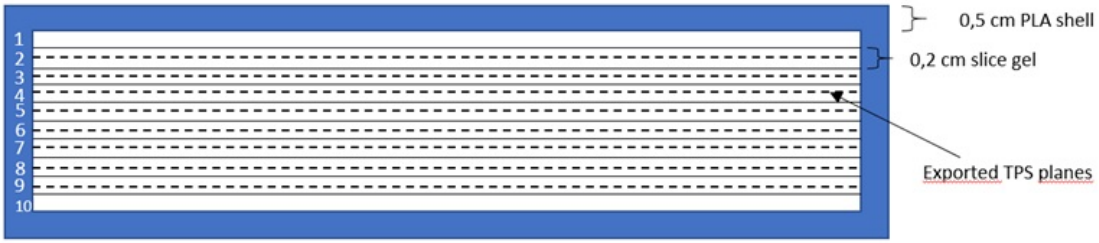

Figure 5.11: Representation of the division of the gel in the cuboid. 10 slices of gel (2 mm) were selected in the gel from which 8 were useful. The dotted lines represent the exported TPS dose planes which were always situated in the middle of the slice of the gel. The numbers of the slices are written next to the corresponding slice.

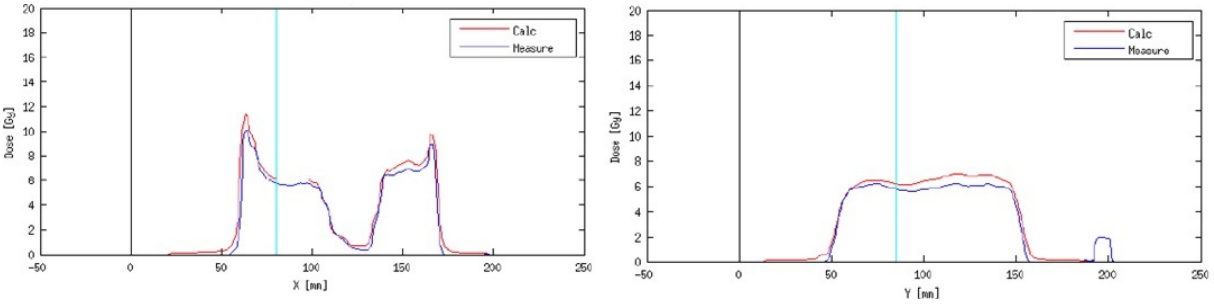

Figure 5.12: Dose profiles measured in slice 3 (0.9-1.1 cm) of the gel (blue) compared to the calculated TPS distributions (red) along the X and Y axis.

This resulted in 8 different γ-scores. Table 5.2 shows these scores for each slice compared to the TPS.

Cuboid B No MRI artefacts were present in these scans resulting in 5 calibration vials (1,2,3,8 and 12 Gy) which could be used for the fitting of the curve. Parameters a, b and c were -2.961, 0.116 and 4.262. Goodness of the fit (R^2) resulted in 0.9999. The calibration curve is shown in figure 5.13.

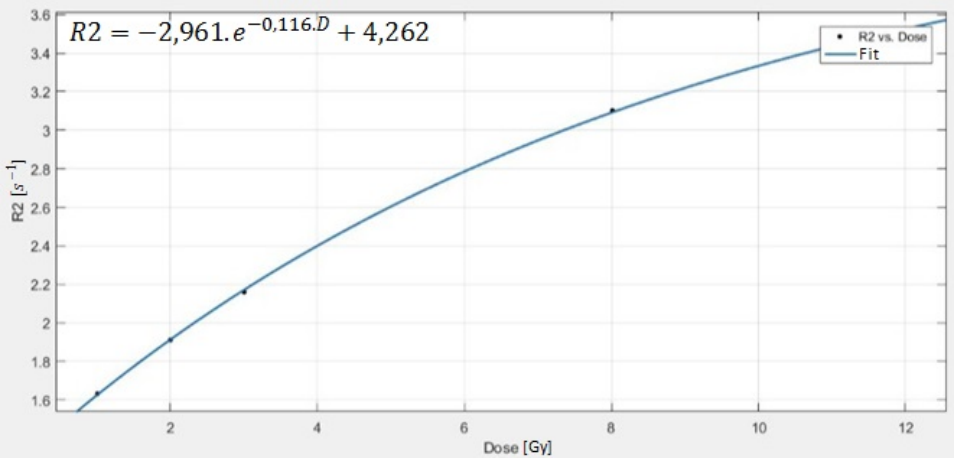

Figure 5.13: Calibration curve linked to cuboid B using the 5 calibration vials. The R_2 value is plotted as a function of the dose.

Comparison to calculated TPS dose planes The same principle is handled as in the previous section with cuboid A of the second run. 8 different γ-scores were obtained from the acquired slices 5.2.

Table 5.2: Calculated γ scores (3%/3 mm) from comparing the gel to the TPS slices. γ scores [%], γ max, γ mean with standard deviation and dose differences [%] were calculated for each slice.

	γ			Dose diff [%]	γ			Dose diff [%]	γ			Dose diff [%]
	Second run, A				Second run, B				Intra-scan, A			
Slice depth [cm]	score [%]	max	mean ±SD	mean ±SD	score [%]	max	mean ±SD	mean ±SD	score [%]	max	mean ±SD	mean ±SD
0.8	22.94	7.82	2.44 ± 1.56	17.26 ± 8.66	12.81	8.57	3.25 ±1.705	19.32 ±5.31	24.34	7.8	2.36 ±1.51	17.03 ±8.66
1	53.08	6.04	1.16 ±0.94	9.38 ±9.14	30.91	7.26	1.73 ±1.21	11.64 ±5.69	56.99	5.04	1.07 ±0.86	8.96 ±9.15
1.2	73.73	5.24	0.73 ±0.70	6.13 ±9.32	45.71	7.52	1.46 ±1.20	9.76 ±5.79	77.77	4.15	0.64 ±0.60	5.58 ±9.32
1.4	87.68	4.54	0.48 ±0.50	3.38 ±9.45	62.08	6.15	0.98 ±0.96	6.02 ±5.86	91.86	3.33	0.41 ±0.39	2.76 ±9.46
1.6	87.69	4.56	0.49 ±0.52	3.29 ±9.43	54.52	6.55	1.22 ±1.15	7.51 ±5.85	90.81	3.4	0.42 ±0.41	2.68 ±9.43
1.8	82.22	4.37	0.58 ±0.56	4.63 ±9.40	51.23	6	1.20 ±1.03	7.91 ±5.23	86.24	3.42	0.50 ±0.46	4.09 ±9.41
2	55.02	5.2	1.04 ±0.77	8.50 ±8.71	26.94	7.2	1.97 ±1.34	12.13 ±4.96	58.96	4.16	0.96 ±0.69	8.07 ±8.74
2.2	30.39	6.49	1.81 ±1.17	13.74 ±8.73	15.06	7.66	2.96 ±1.63	16.88 ±4.71	32.16	5.67	1.73 ±1.12	13.45 ±8.76
Slice depth [cm]	Intra-scan, B				Inter-scan, A				Inter-scan, B			
0.8	11.61	9.2	3.63 ±1.85	20.63 ±5.19	18.13	8.6	2.99 ±1.83	19.79 ±8.38	16.5	7.79	2.64 ±1.46	16.75 ±5.50
1	24.44	7.96	2.07 ±1.38	13.22 ±5.62	36.33	6.87	1.61 ±1.18	12.17 ±8.85	49.86	6.44	1.24 ±1.00	8.83 ±5.88
1.2	35.46	8.21	1.79 ±1.38	11.40 ±5.77	54.07	6.09	1.14 ±0.92	9.01 ±9.02	59.49	6.7	1.01 ±0.98	6.89 ±5.98
1.4	53.69	6.91	1.23 ±1.18	7.78 ±5.87	71.45	5.41	0.79 ±0.73	6.36 ±9.14	71.79	5.29	0.73 ±0.72	3.03 ±6.06
1.6	46.96	7.29	1.50 ±1.36	9.21 ±5.88	72.49	5.43	0.78 ±0.75	6.27 ±9.12	63.85	5.71	0.92 ±0.87	4.56 ±6.04
1.8	43.8	6.76	1.51 ±1.22	9.59 ±5.24	63.43	5.23	0.93 ±0.80	7.58 ±9.10	33.47			
2					37.18	6.06	1.49 ±1.01	11.32 ±8.43	43.24	6.38	1.45 ±1.12	9.34 ±5.12
2.2	12.9	8.32	3.33 ±1.79	18.27 ±4.63	23.72	7.32	2.31 ±1.44	16.39 ±8.43	20.33	6.85	2.36 ±1.39	14.24 ±4.87
Slice depth [cm]	Inter-scan 14 vials, A				Inter-scan 14 vials, B							
0.8	39.25	5.56	1.86 ±1.50	15.04 ±12.15	47.42	6.03	1.47 ±1.32	12.10 ±10.55				
1	79	2.46	0.63 ±0.54	4.29 ±13.53	73.76	2.94	0.6 ±0.45	0.50 ±12.47				
1.2	97.04	4.53	0.37 ±0.29	0.15 ±14.2	84.53	4.16	0.53 ±0.49	3.73 ±11.64				
1.4	85.2	3.42	0.54 ±0.40	3.85 ±16.19	62.18	7.05	0.92 ±0.75	9.83 ±13.41				
1.6	86.19	2.56	0.53 ±0.40	3.84 ±15.38	75.4	4.71	0.69 ±0.58	6.66 ±10.74				
1.8	94.44	1.69	0.39 ±0.31	2.13 ±14.90	79.28	4.77	0.62 ±0.56	5.92 ±11.67				
2	84.5	2.24	0.56 ±0.41	3.18 ±13.59	84.65	2.18	0.56 ±0.4	1.19 ±10.51				
2.2	47.84	4.82	1.26 ±0.95	10.40 ±13.05	51.69	5.04	1.25 ±1.05	8.67 ±10.55				

5.2.2 Second run: intra-scan study

Both cuboids from the second run were also converted by calibration curves taken from a slice which was located less deep (from the same scan). This was done to evaluate the variance in R_2 and the impact on the results. The number corresponding to each slice can be found in figure 5.11).

Cuboid A In section 5.2.1 slice 6 was chosen to select the ROIs to attain the mean R_2 values and the standard deviations (SDs). In this section slice 5 (figure 5.11) from cuboid A was taken to calculate the calibration fitting parameters. Again the calibration vial of 8 Gy was left out.

Parameters of the calibration curve resulted in a=-2.81, b=0.1237 and c=4.088 with R^2 being 0.9999 (figure 5.14).

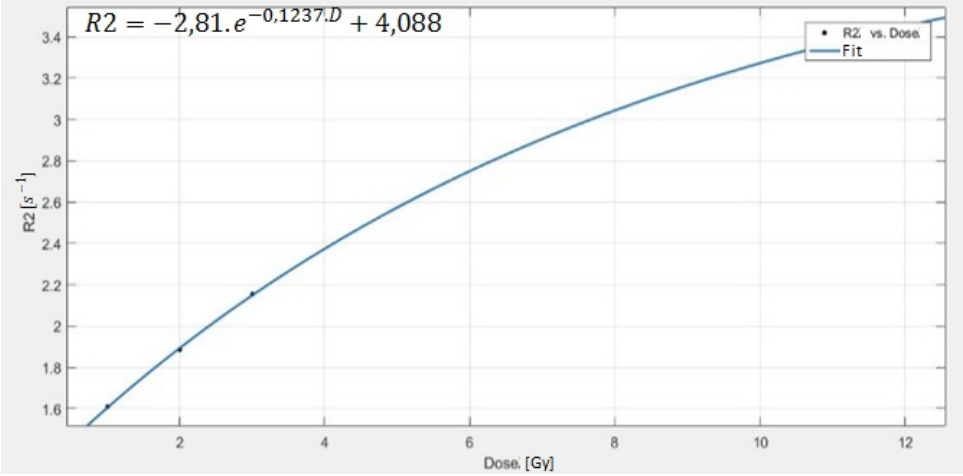

Figure 5.14: Calibration curve linked to cuboid A, at slice 5, using the 4 calibration vials. The R_2 value is plotted as a function of the dose.

Comparison to calculated TPS exported dose planes Calculated γ-scores when compared to the TPS dose planes can be found in table 5.2.

Cuboid B In the second run cuboid B was calibrated using slice 7 within the phantom. In this intra-scan study slice 5 was used to calibrate the R_2 maps from the gel. Fitting parameters resulted in a=-3.02, b=0.1154 and c=4.315 (figure 5.15).

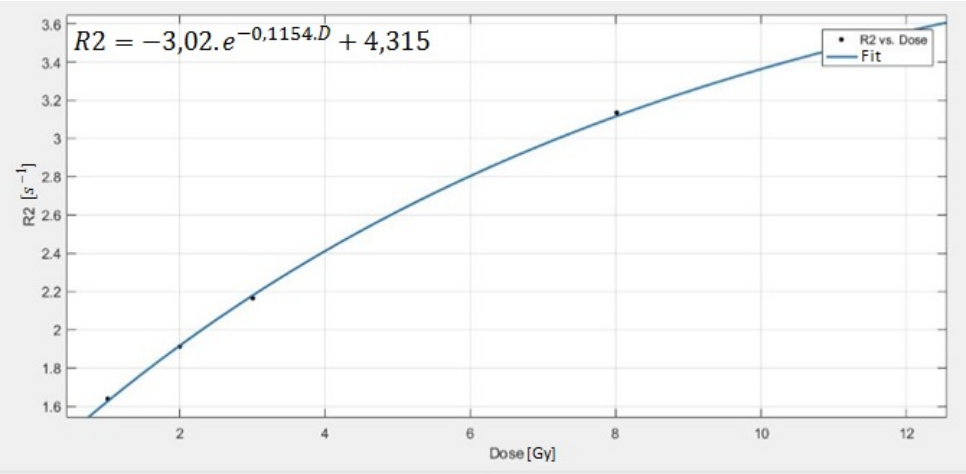

Figure 5.15: Calibration curve linked to cuboid B, at slice 5, using the 5 calibration vials. The R_2 value is plotted as a function of the dose.

Comparison to calculated TPS exported dose planes Corresponding parameters and γ-scores can be found in table 5.2.

5.2.3 Second run: inter-scan study

In this study calibration curves from A and B were switched. More specifically cuboid A was matched with the calibration curve from cuboid B located at slice 7. Cuboid B was matched with the one from A at slice 6.

Because of the high similarity between these 2 curves the calibration curves were reassessed for both cuboids. This way an additional test could be performed. R_2 values and their standard deviations are written down in table 5.3.

Table 5.3: R_2 values with standard deviations are displayed for cuboid A and B.

A		B	
R_2 [s^{-1}]	SD [s^{-1}]	R_2 [s^{-1}]	SD [s^{-1}]
1,6152	0,0114	1,6324	0,0083
1,9007	0,0226	1,9038	0,0069
2,1469	0,0211	2,1585	0,0081
		3,1	0,0505
3,4705	0,0916	3,4799	0,064

Cuboid A This print was combined with the calibration curve from cuboid B positioned at slice 7. Calibration parameters were already defined in section 5.2.1, figure 5.13.

Comparison to calculated TPS exported dose planes γ calculations can be found in table 5.2.

Cuboid B Cuboid B was matched with the calibration curve from cuboid A located at slice 6. Calibration parameters have already been defined in section 5.2.1 and figure 5.10.

Comparison to calculated TPS exported dose planes Distribution results can be found in table 5.2.

5.2.4 Second run: inter-scan study using third scan with calibration vials

Gel dosimetry

A second inter-scan study involved 14 calibration vials from the third scan. The resulting calibration function was applied to cuboid A and B. More calibration data should result in a better conversion from R_2 maps to dose.

Parameters of the fit were a=-2.116, b=0.1891 and c=3.402 with an R^2 of 0.9977. Figure 5.16 shows the mono-exponential fit.

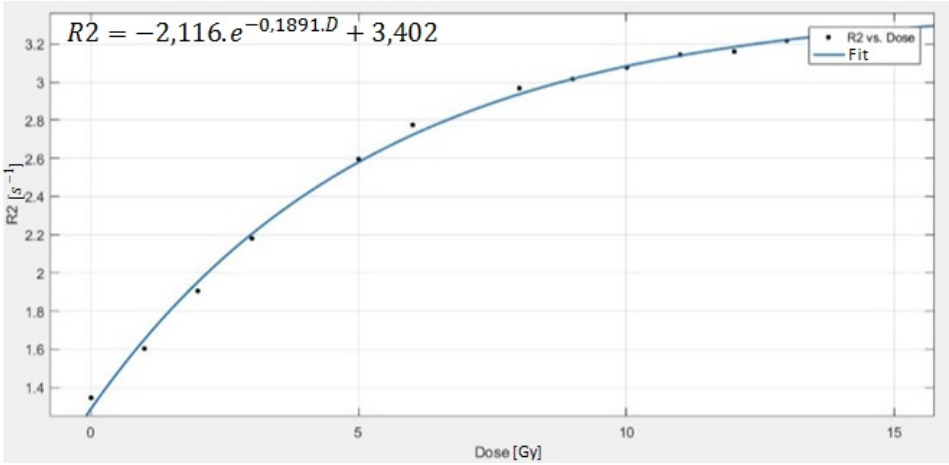

Figure 5.16: Calibration curve linked to the third scan involving 14 calibration vials. The R_2 value is plotted as a function of the dose.

Cuboid A: comparison to calculated TPS exported dose planes This section underwent the same procedure for the TPS plane selection as the previous sections. Table 5.2 represents the data.

Cuboid B: comparison to calculated TPS exported dose planes Data is represented in table 5.2. Figure 5.17 displays the γ and dose distributions for cuboid A and B which were calibrated with 14 vials.

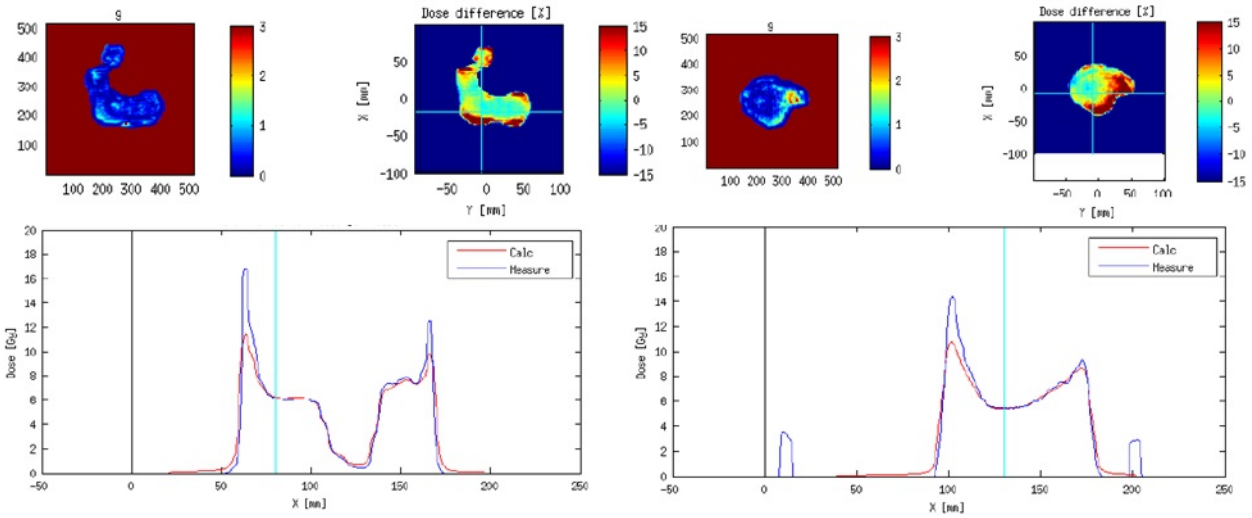

Figure 5.17: The fourth slice is represented here. The calculated dose distribution (TPS) is compared to the measured distribution inside the gel (blue). Left: cuboid A, right: cuboid B. Both are calibrated using 14 calibration vials from the third scan. Dose profiles along the X axis are also shown.

Film dosimetry

EBT3 film was placed in between water equivalent RW3 plates at 10 mm and 20 mm for both cuboids A and B.

Cuboid A: EBT film at 10 mm The results included an agreement score (3%/3 mm) of 44.81%, a max γ value of 5.89 and a mean γ of 1.31 $\pm$0.97. Dose difference [%] measured a median value of 13.08 while the mean value and SD were 14.03 $\pm$16.57.
Figure 5.18 displays the dose distributions from cuboid A and the film, the γ distribution and the dose difference map.

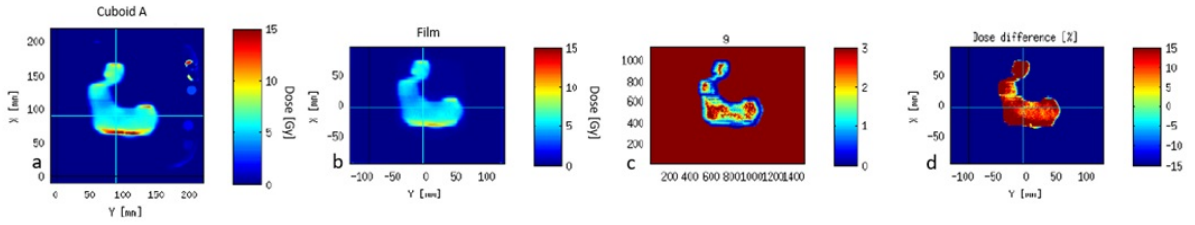

Figure 5.18: a) averaged dose plane from A, b) EBT3 film at 10 mm depth, c)γ distribution and d) dose difference.

Cuboid A: EBT film at 20 mm An agreement score (3%/3 mm) of 93.68% was observed. A maximal γ of 33.33 and mean value with SD of 0.42 $\pm$0.34 were calculated. Dose differences [%] included a median value of -0.81 and mean value with SD of 0.35 $\pm$12.01.
Dose, γ and dose difference distributions are illustrated in figure 5.19). Dose profile lines along the blue lines are presented in figure 5.20.

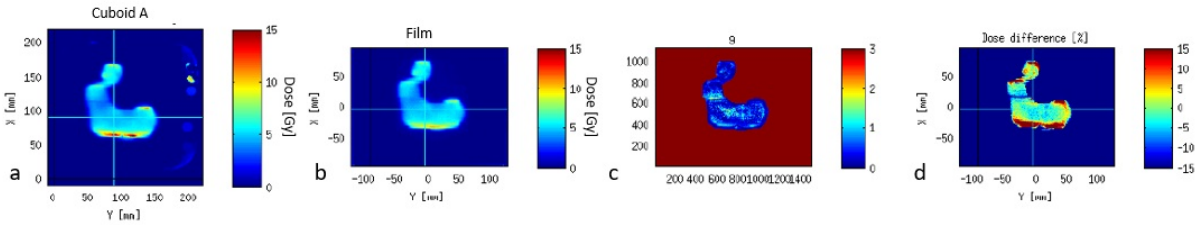

Figure 5.19: a) averaged dose plane from A, b) EBT3 film at 20 mm depth (RW3), c) γ distribution and d) dose difference.

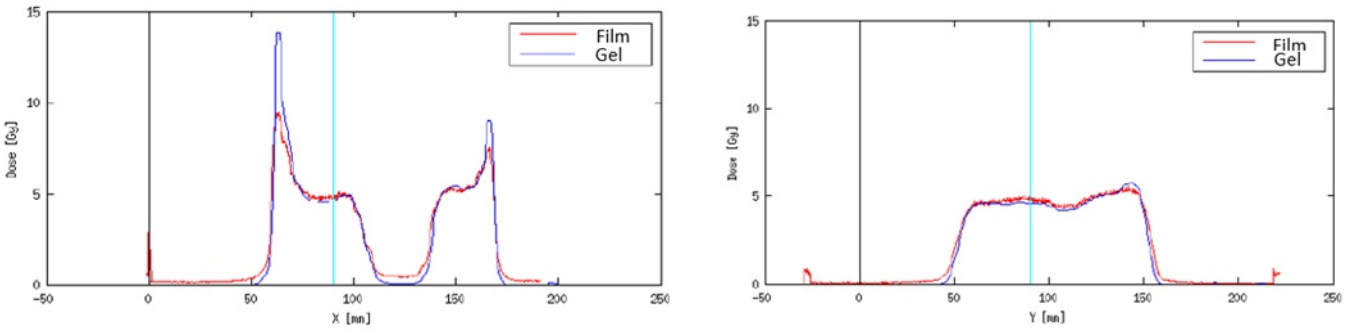

Figure 5.20: Dose profiles along the X and Y axis of cuboid A: figure **??**.

Cuboid B: EBT film at 10 mm The agreeemnt score (3%/3 mm) resulted in 55.21%. Mean γ with SD were 1.24 $\pm$1.11 were attained. The dose difference [%] presented a median of -9.71 and mean with SD of -8.71 $\pm$13.63. Distributions are displayed in figure 5.21).

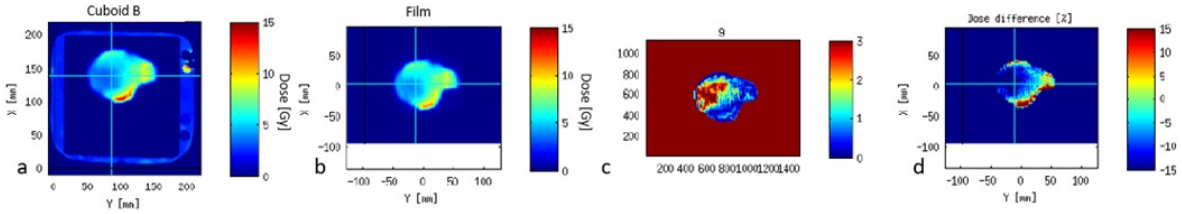

Figure 5.21: a) averaged dose plane from B, b) EBT3 film at 10 mm depth (RW3), c)γ distribution and d) dose difference.

Cuboid B: EBT film at 20 mm The γ (3%/3 mm) showed an agreement of 80.64%. Maximal g: 3.69, mean with SD: 0.60 $\pm$0.46, median dose difference [%]: -1.96 and mean with SD of -0.08 $\pm$10.22. Distributions can be found in figure 5.22. Dose profile lines along the blue lines of figure 5.22 are presented in figure 5.23.

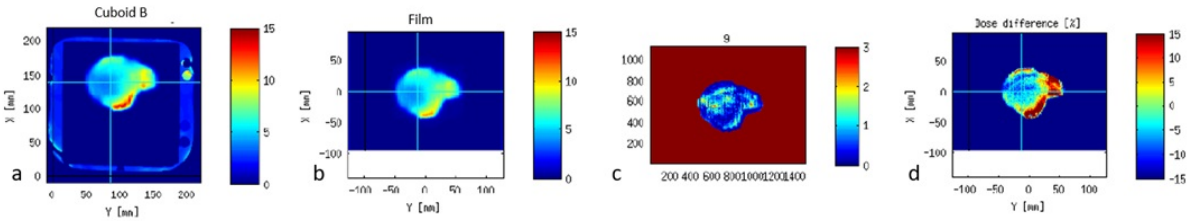

Figure 5.22: a) averaged dose plane from B, b) EBT3 film at 20 mm depth (RW3), c)γ distribution and d) dose difference.

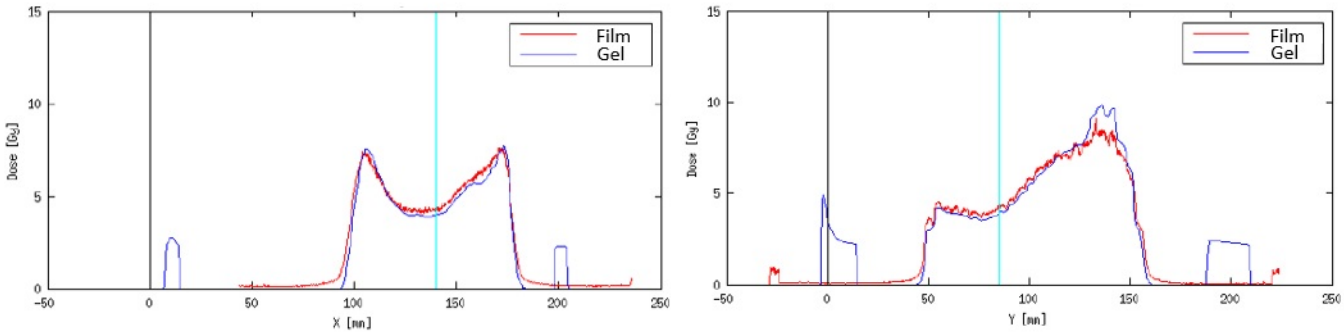

Figure 5.23: Dose profiles along the X and Y axis of cuboid B: figure 5.22.

5.3 Discussion

5.3.1 Second run

Cuboid A A good exponential fit was found between the calculated R_2 values. When looking at the data from table 5.2 a first trend could be observed: slices near the PLA shell typically have a lower agreement score. The dose registered in these surfaces of the gel reveal a lower dose than calculated by the TPS. This seems to be an effect of the diffused oxygen into the print. The fact that bad scores are observed near both sides of the PLA shell indicates the diffusing of oxygen inside the print which can inhibit the polymerization process. Figure 5.12 shows the dose profile lines where can be seen that the gel (blue) exhibit less dose than the calculated distribution (red). A lower dose is measured throughout almost all slices. It appears that if a normalization method would be applied, better results would be obtained [11].

The agreement score increments till slice 6 after which it decreases again. This has probably to do with the dose maximum, which is approximately at 1.5 cm for a 6 MV beam. Slice 5-7 range from 1.4 cm till 1.8 cm in depth. In this region the gradient of the dose is less steep. Going from slice 2 till 9 no excessive overshoots were observed.

Cuboid B The dose distributions registered in the gel were for all slices lower than the calculated TPS distributions. This could also be explained by the oxygen effect. Due to certain circumstances during fabrication the print was only able to be filled for about 3/4 of its content resulting in an oxygen reservoir inside the print which in turn allows more to be infiltrated in

the gel (figure 5.24).

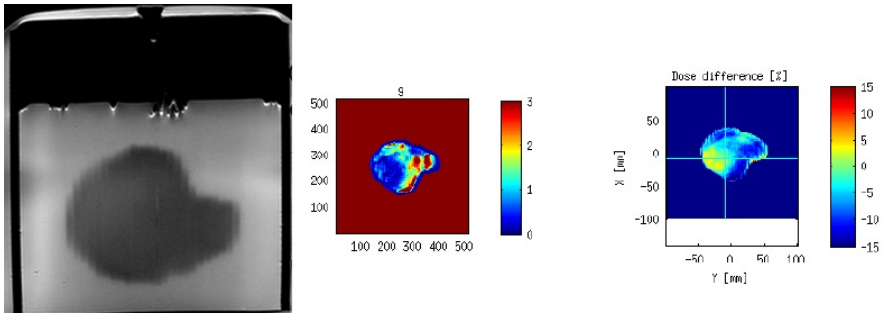

Figure 5.24: A MRI slice of cuboid B. Clearly the cuboid is only filled for about 3/4. The γ distribution and dose difference [%] are also displayed.

5.3.2 Second run: intra-scan study

Cuboid A The calibration curve obtained from slice 6 was used in section 5.2.1 while the function slice 5 was presented in section 5.2.2. Slightly better results were observed by calibrating the R_2 maps with the function from slice 5. Each slice has approximately a 3% higher score. Figure 5.25 represents the two fitted calibration curves at different depths. The function from slice 5 is less steep which results in a slightly higher dose in the range from 7 till 12 Gy. This small improvement in dose difference can be seen in figure 5.26.

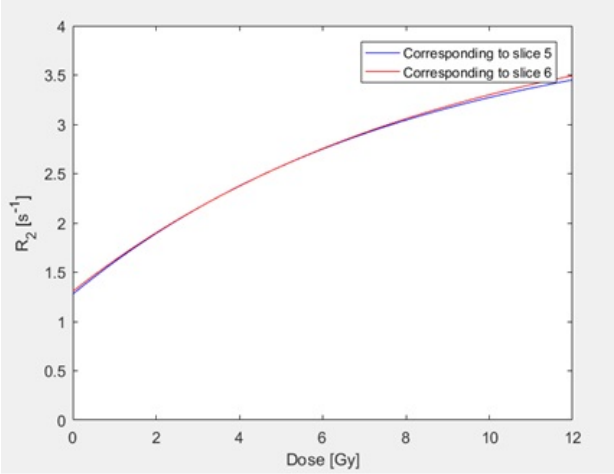

Figure 5.25: Representation of the two fitted calibration curves from slice 5 and 6 in cuboid A.

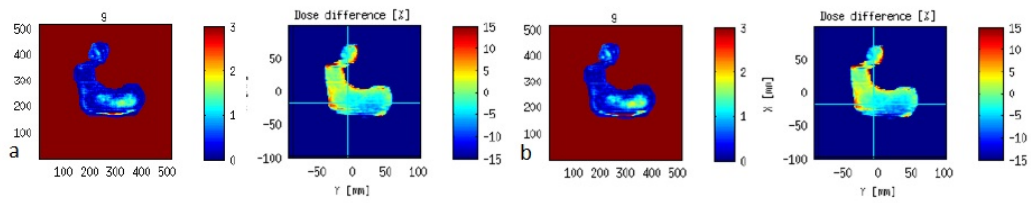

Figure 5.26: a) γ and dose difference [%] distributions from slice 5 calibration, b) γ and dose difference [%] distributions from slice 6 calibration.

Cuboid B The same principle was handled here: the calibration function originating from slice 7 (section 5.2.1) was compared to the one plotted from slice 5 (section 5.2.2). The scores presented in the both tables show a difference of roughly 5-10% in agreement scores. In this case the function from slice 7 corresponds to a higher dose for the same R_2 values.

This section indicates that calibration functions coming from the same scan, but taken at another depth result in an altered γ score.

5.3.3 Second run: inter-scan study

The calibration function from cuboid B applied to A resulted in lower γ scores. An averaged difference of 15% in γ scores was observed. Figure 5.27 displays both functions. Recall that cuboid A only has 4 calibration vials while cuboid B has 5. It appears when the omitted vial from cuboid A is replaced by the one from cuboid B, similar graphs are obtained.

Parameters derived from the selected ROIs from cuboid A and B are displayed in table 5.3. Figure 5.27 is obtained if the omitted vial in A is replaced by the corresponding value in B. It seems that both curves are nearly equal.

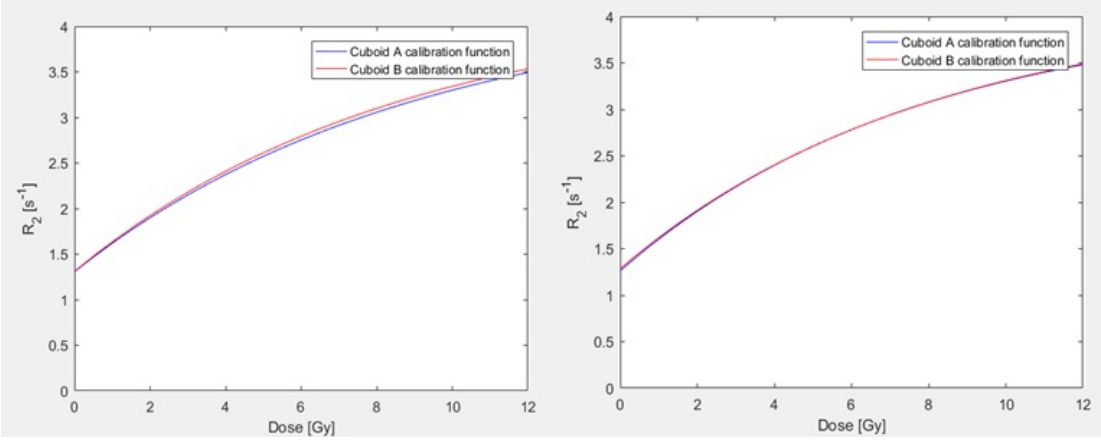

Figure 5.27: Calibration functions from cuboid A and B. Left: original calibration functions for the second run, right: if the omitted R_2 is replaced by the one obtained in B.

5.3.4 Second run: inter-scan study using third scan with calibration vials

Gel dosimetry

Cuboid A and B were also calibrated using the third scan with 14 calibration vials. When comparing these γ scores to the scores obtained by other calibration functions it was found that most of the time these resulted in higher scores as well for cuboid A and B.

For both cuboids the first and last slice (2 and 9) were characterised by a measured dose which was lower than the calculated TPS distributions. Again, this points in the direction of the influence of oxygen which in lower concentrations inhibit the polymerization process of the monomers.

The γ scores are better, but the overshoots become more prominent and severe when compared to the previous functions. Both slices present in figure 5.17 were calibrated using the third scan. γ score analysis (3%/3 mm) resulted in 97.04% for cuboid A and 84.53% for B.

A good agreement was found for both but the displayed overshoots are relatively large. The discussion of the preliminary study already mentioned some variables which could influence these overshoots: temperature drift and steep dose gradients.

Temperature drift is assumed to be the most outstanding factor because all the MRI scans were performed in the same water tank. As a result the temperature of the water was already increment at the beginning of the third scan. Figure 2.11 shows that an increased temperature lowers the curve and results in a higher dose. Figure 5.28 displays the calibration functions for A,B and the third scan. For higher doses this phenomenon becomes more excessive: 12 Gy measured approximately 3.50 s^{-1} for scans in cuboid A and B while 12 Gy in the third scan results in nearly 3.17 s^{-1}. This is probably the main cause of the huge overshoots. Other factors that could have contributed are explained in the next few paragraphs.

Steep dose gradients also result in overshoots. Vergote K. *et al.* explained in their paper that a high dose region results in a depletion of monomers. In this high dose region long living macroradicals are created. Monomers from the adjacent low dose region diffuse into the high dose region and interact with these macroradicals which gives overshoots in steep dose gradients [45].

Dose overshoots near the edges of the field are also dependent on the penumbra width (defined between 10% and 90% of the maximal dose). However the paper mentioned a relative maximal dose overshoot of less than 5% for doses of 12 Gy [45].

Another interesting article by Karlsson A. *et al.* showed the dependence of a gel dosimeter on sequential beam irradiation. The applied method included a time interval of 70 s in between the beams. The paper concluded that higher R_2 values for the same absorbed dose were measured when fractionation was applied. This effect becomes more prominent when a higher total dose is given [59]. In our experiment the field was applied 9 or 10 times. The time in between fields corresponded to the MLC leaves which needed to be brought back to their starting position before a new field could be applied.
It is therefore assumable that a combination of the above mentioned factors is the cause of these great overshoots. The calibration curve with 14 vials also appears to go into saturation near a dose of 12 Gy what also influences the conversion to dose. This effect is due to the temperature drift during scanning [11].

This calibration function has the best overall γ-scores, but also the most prominent overshoots. However, this would not seem to be the best calibration function. The effect of the temperature drift is too large to be able to compensate with a normalization method. The fact that the results in the second run (section 5.2.1) do not exhibit large dose overshoots points out that the most contributing factor is the temperature drift during the third scan. Better results would be obtained if a normalization method would have been applied to cuboid A from the second

run [11]. Dose profile lines for slice 3, 4, 5, 6 and 7 for cuboid A during the second run (5.2.1) are displayed in the appendix section 'Dose profile lines from cuboid A, second run' to illustrate this.

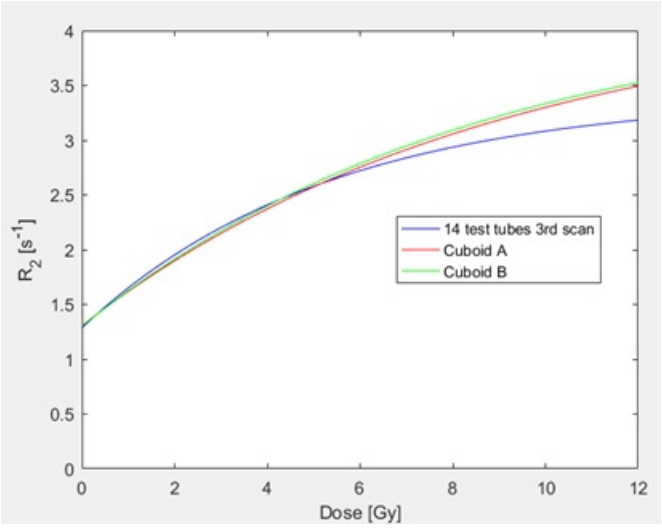

Figure 5.28: Plotted calibration functions from cuboid A, B and the third scan with 14 vials.

Film dosimetry verification

Film dosimetry confirmed the comparison of the gel to the TPS calculated dose distributions. Measurements at 10 mm depth for both cuboids resulted in poor scores. Measurements at 20 mm depth, when corrected for the 0.5 cm PLA shell yielded good results for cuboid A. Figures 5.20 and 5.23 show the dose profile lines along figures 5.19 and 5.22 respectively.

Chapter 6

General discussion

The performance of the gel would be improved if the diffusion of oxygen inside the print could be avoided [42]. In the executed experiments the gel was poured into the 3D print, sealed with a plastic lid and directly placed in a water tank at 32°C to assure a similar cooling trajectory. Somewhere along the way oxygen was able to diffuse inside the print.

An improved accuracy is obtained when assessing multiple calibration vials in the desired dose region. It is advisable to obtain more than 5 calibration vials and scan them together with the phantom. Otherwise temperature drift could cause the calibration curve to deviate as smaller R_2s for the same dose are registered resulting in a higher converted dose. This effect is assumed to be the main cause of the large overshoots measured in the inter-scan with 14 calibration vials. In these experiments absolute dosimetry was performed [40]. The fabrication of a hybrid 3D printed bolus for normalization purposes could improve the accuracy. Normalization has been suggested by several articles [11] to reduce overestimations and overshoots. This could be done by inserting a point detector.

In these experiments doses till 12 Gy were given to the phantom. It could be that more long-lived macroradicals are being created near higher rates of polymerization [45]. Maybe when less dose is absorbed, these overshoots would also decrease in size. Polymer gel also exhibits a dependence on sequential beam irradiation. It could be possible that by applying the same field 9 or 10 times this could also have had an effect.

The original goal of this study was to insert PAGAT polymer gel in a 3D printed bolus. However in the performed studies involved printed cuboids. If the gel would be inserted in a patient specific bolus, some practical properties must be considered.

Mechanical firmness was mainly established due to the thick walls of the print, these were 0.5 cm. Current boluses used in radiotherapy have an average thickness of 1-2 cm. An alternative method could be the printing of infill support structures which would attach the outer walls resulting in a more firm structure. This could reduce the number of layers present in the contours. A second consideration should be the limitations which are introduced by the MRI read-out. Temperature drift during read-out is a major concern. It is therefore advised by several papers such as [40, 60] to implement active temperature-controlled conditions. Another possible limitation is the volume of the 8-channel head coil. In the present study a plastic water tank of

dimensions 19x19x8 cm^3 was already a tight fit. The fact that calibration vials and the bolus need to be scanned together to minimize temperature drift and the available volume results in limited space. The arrangement of the calibration vials and the bolus in the water tank should be put in such a way that each taken slice possesses them together. This would also reduce the MRI read-out time. An average time of 30-40 minutes was recorded to assess 10 consecutive slices of 2 mm thick.

Chapter 7

Conclusion

Experiments demonstrated the homogeneity of the polymer gel. Also PLA was found to have a higher relative electron density than water while the gel is nearly water equivalent. It has been shown that it is feasible to gain a proper dosimetric signal from the PAGAT polymer gel from inside a 3D print. However experiments illustrated that there are parameters which must be taken into account.

The first and last layers of the gel showed an indication of O_2 infiltration in the print. All cuboids were placed in a water tank directly after fabrication, but apparently this was not sufficient to avoid the diffusion of oxygen. Overestimations of the dose can be attributed to the temperature drift during MRI read-out. It has been shown in several articles [8] that a small offset between the calibration vials and the phantom could result in large dose deviations. Using just a water tank which was placed in a head coil will probably not have been satisfactory to achieve clinical acceptable results.

Best γ scores were obtained using the third scan with 14 calibration vials to convert the R_2 maps from the gel to dose. Highest scores were measured at slice depths ranging from 1.3 cm till 2.1 cm in depth from which one was 97.04%. However dose overshoots were more pronounced, due to temperature drift, and appear near high dose gradients. If the proposed normalization method by Vandecasteele J. [11] would've been applied to the calibration function of the second run, this section (5.2.1) could have had the best overall results without such excessive overshoots as in the section with 14 calibration vials.

The fabrication of the gel was easily assessed during the experiments. Care must be taken when working with Aam and Bis which are neurotoxic and carcinogen. A drawback is the protocol which must be followed to assure a similar cooling trajectory after fabrication ($\pm$24 h in a water tank) and the time to let the gel stabilize in between irradiation and MRI read-out (at least 12 houres). A future difficulty would be the availability of the MRI scanner. During the performed experiments the entire time scheduled protocol of fabrication and irradiation needed to be adapted to the availability of the MRI scanner.

Appendix

Time schedule protocol for fabrication, irradiation and read-out

Day 1: fabrication of the polymer gel

Time frame

- Start at least at 13 o'clock at the laboratory of experimental radiotherapy and oncology.
- Expected ending time fabrication process: 16-17 o'clock.
- After which the gel must be immediately stored in a plastic water tank at 32 °C.

Materials

- 2 erlenmeyer flasks (of 1l or 2 l), 2 magnetic stirrers (and heaters).
- A thermometer
- Weighing scale
- 3D print, calibration tubes and syringe of 60 ml.

Gelatine solution

- Add 60,00 g of gelatine to 440,00 ml deionized water at room temperature.
- Stirr moderate (gelatine doesn't solve too good in cold water).
- Slowly heat the solution till maximal 45°C. Preferred: 40°C.

Acrylamide solution

- Add 30,00 g acrylamide (Aam) to 440,00 ml deionized water (good solubility).
- Add Bis to acrylamide solution with constant stirring ('full power').
- After addition, heat the solution to a certain 60°C (to improve the solving of the Bis).
- Let the solution cool down to a 40-50°C.

Combination of the solutions

- Combination may occur between 40-50°C. Both solutions having the same temperature is desirable.

THPS

- Add 2,12 ml or 2,904 g THPS at 32°C. (The exact temperature is of the most importance here).
- The solution only stays in a liquid state for 10 minutes after the addition of THPS.

Cooling down

- Pour gel in the bolus and calibration tubes (use a 60 ml tube to insert in bolus).
- Shut 3D print with a small lid and superglue.
- Print and calibration vials need to be stored together in a water tank which has a temperature of 32°C to assure similar cooling trajectory.
- Let the water acclimatize to room temperature. Make sure 20-24 houres are present between fabrication and irradiation.

Remarks

- Aam is neurotoxic and is carcinogen. Bis causes irritations.
- The entire process of fabrication should be held under a fume hood.

Day 2: irradiation of the batch

Timeframe

- At 15h take the bolus and calibration vials out of the water tank.
- Irradiation takes place at 16h.

Irradiation

- Get the prints out of the water at 15h (1h before irradiation).
- At 16h a CT scan must be taken with the bolus on top of the RW3.
- Irradiate the calibration tubes to well-defined doses.

  Radiochromic film should be placed between the bolus and RW3.

  Radiochromic film measurement at a certain reference depth (as if it would be placed in the bolus).

  A radiochromic film after dose maximum could be usefull as a reference for the attenuation of the bolus.
- Irradiate bolus, phantom and radiochromic film with an IMRT plan.
- Afterwards store in the MRI room where read-out will take place (to prevail temperature swings).

Day 3: polymer gel read-out

Time frame

- Read-out between 13h (20h waiting time) or read-out at 17h (24h waiting time).

MRI

- Place phantom within the coil
- Calibration vials need to be read-out surrounded by water to prevent temperature offsets between calibration vials and the phantom.

Post processing of the acquired MRI images

Use the inhouse matlab code of dr. ir. Vandecasteele to obtain the dose-R_2 maps.

Dose profile lines from cuboid A, second run

In this section the dose profile lines along the X and Y axis from cuboid A in the second run are presented for slice 3,4,5,6 and 7. The γ and dose difference distributions are also present.

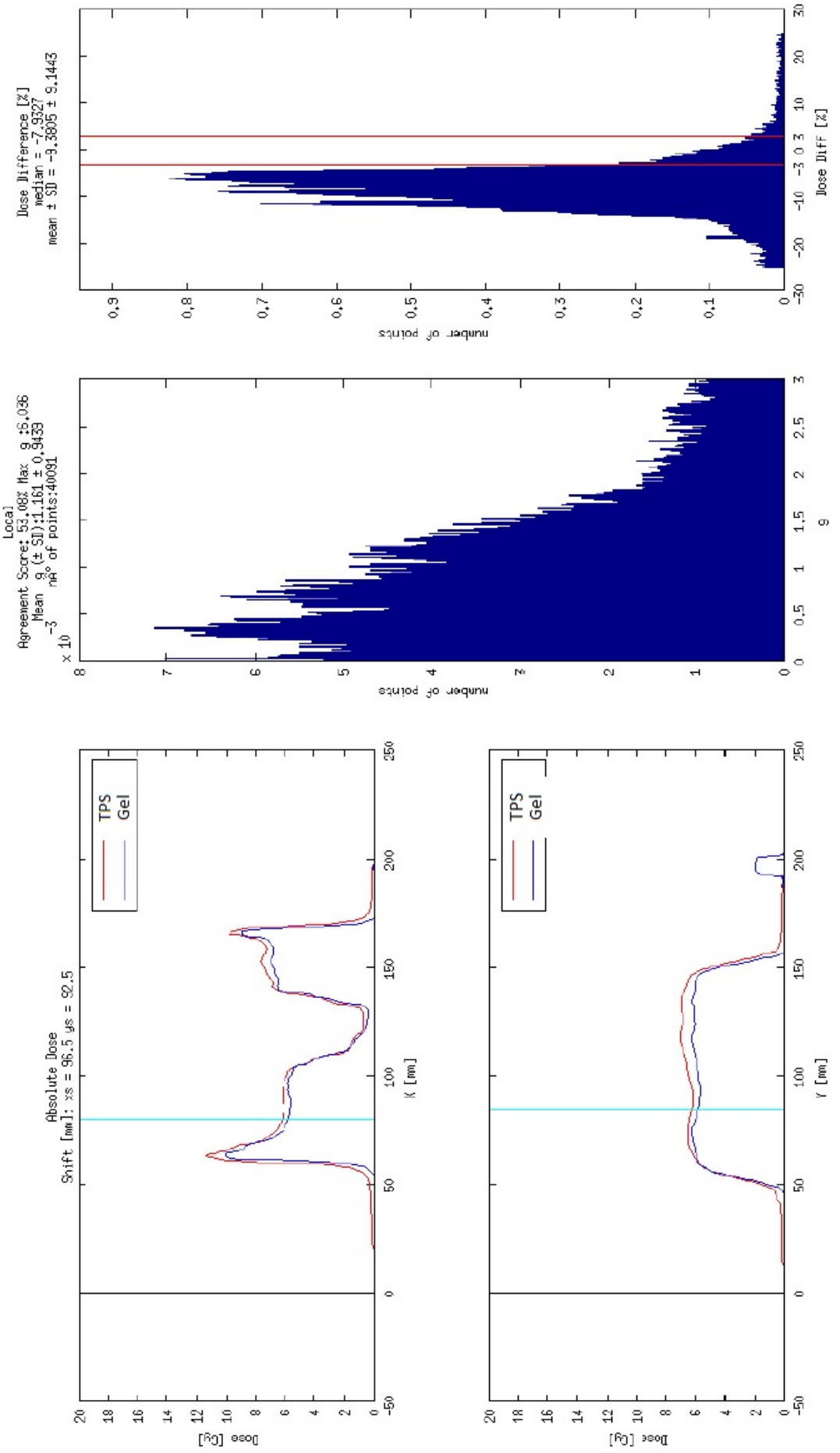

Figure 1: Dose profiles from cuboid A in the second run, slice 3.

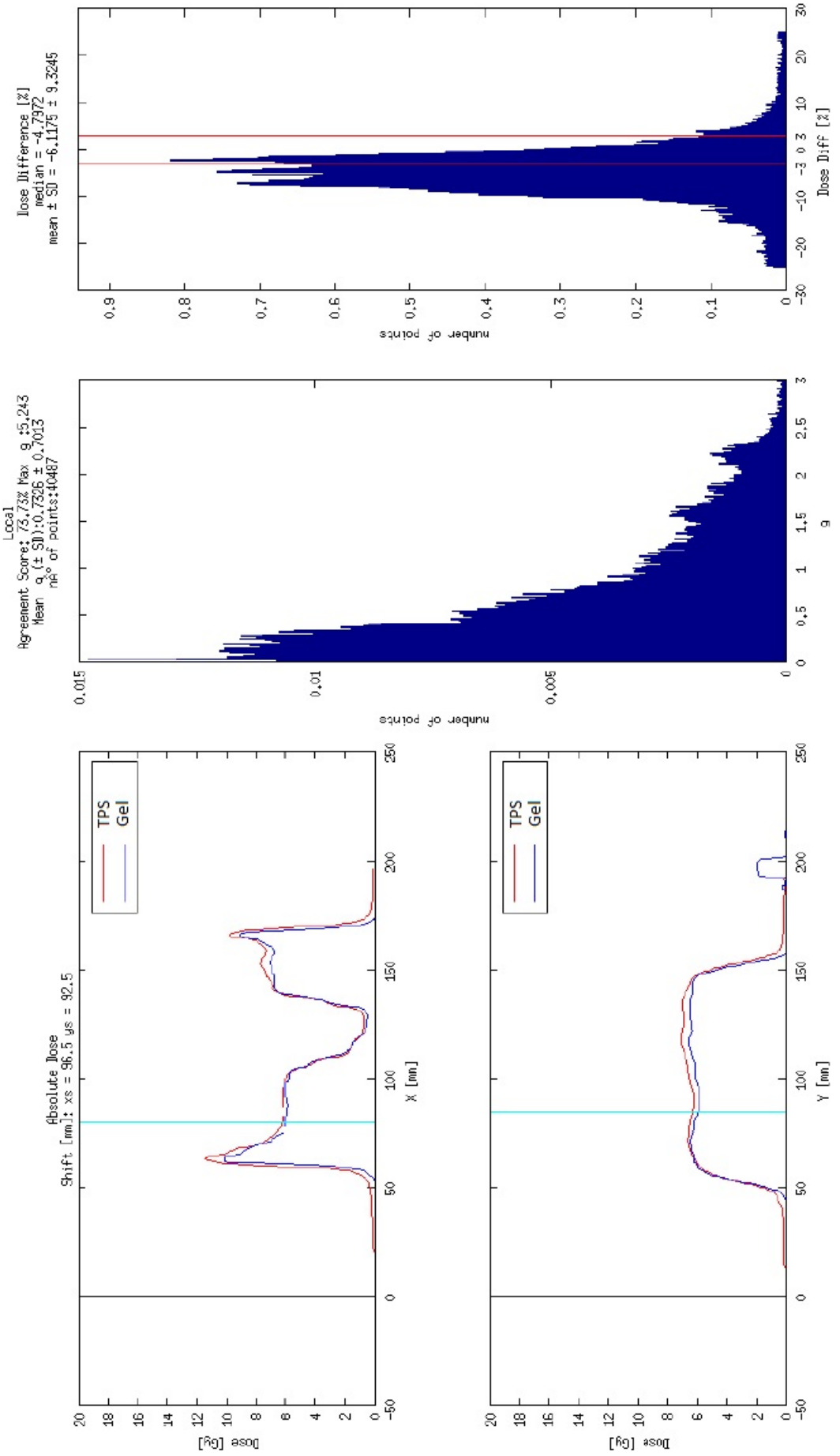

Figure 2: Dose profiles from cuboid A in the second run, slice 4.

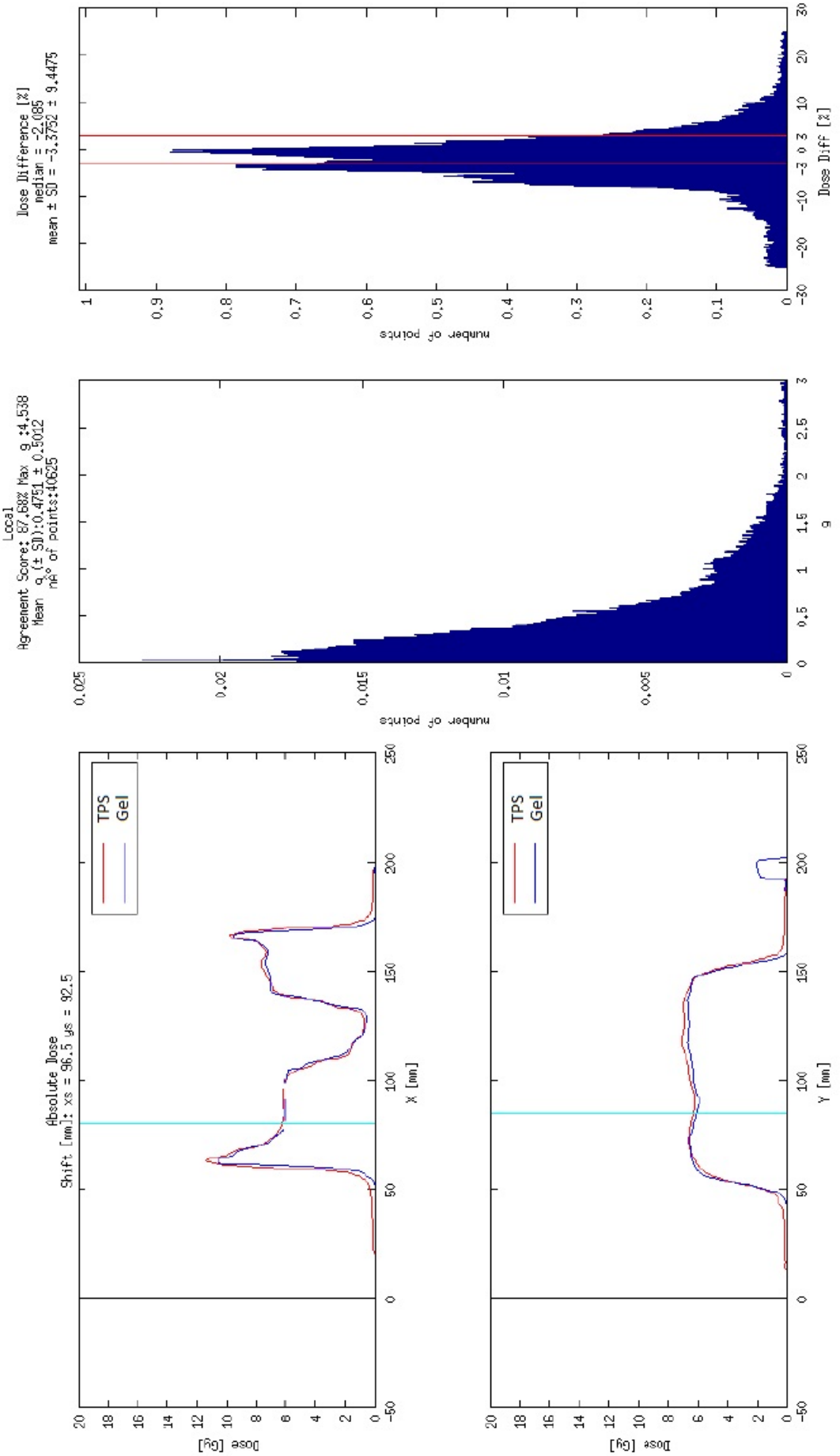

Figure 3: Dose profiles from cuboid A in the second run, slice 5.

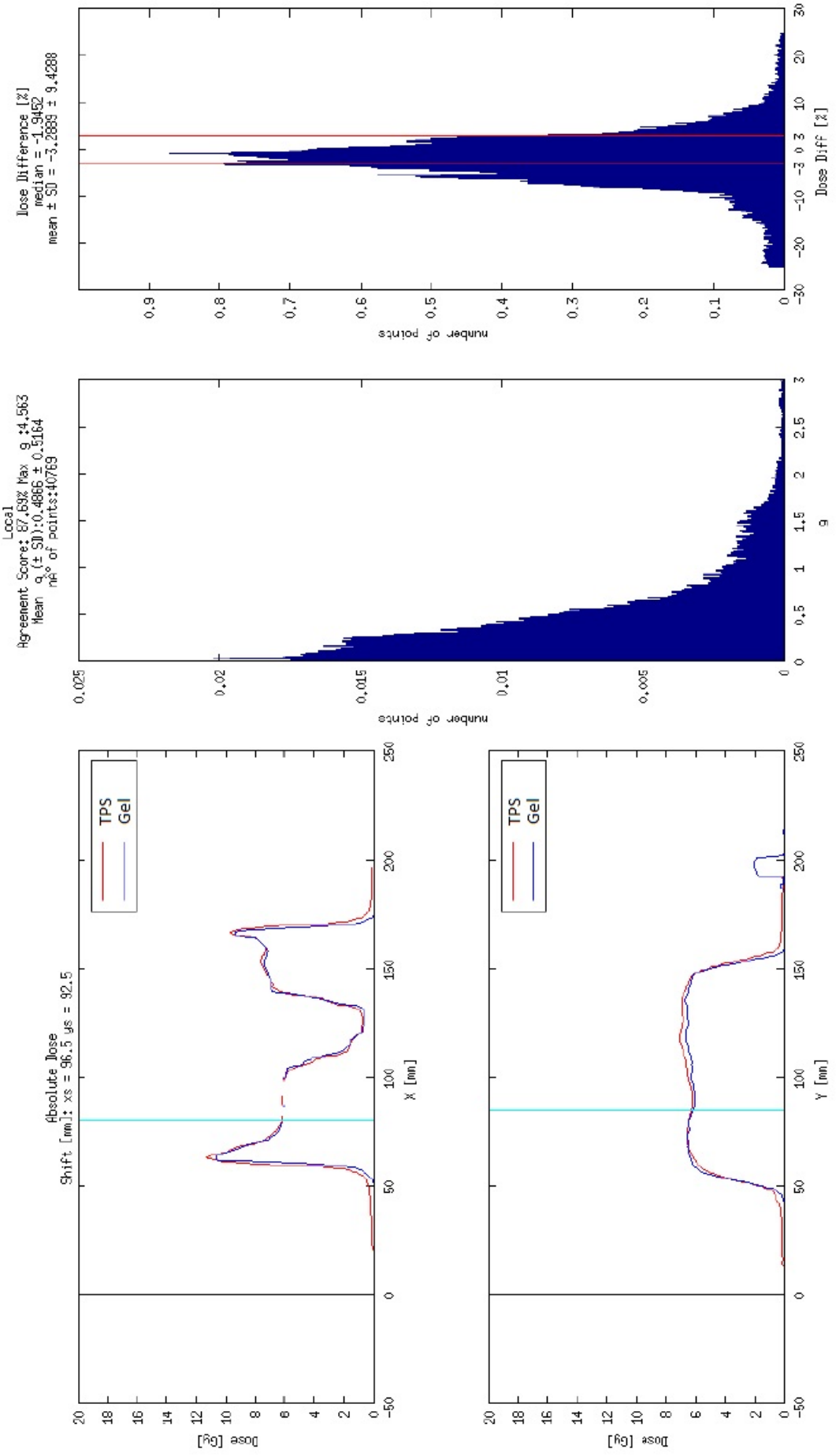

Figure 4: Dose profiles from cuboid A in the second run, slice 6.

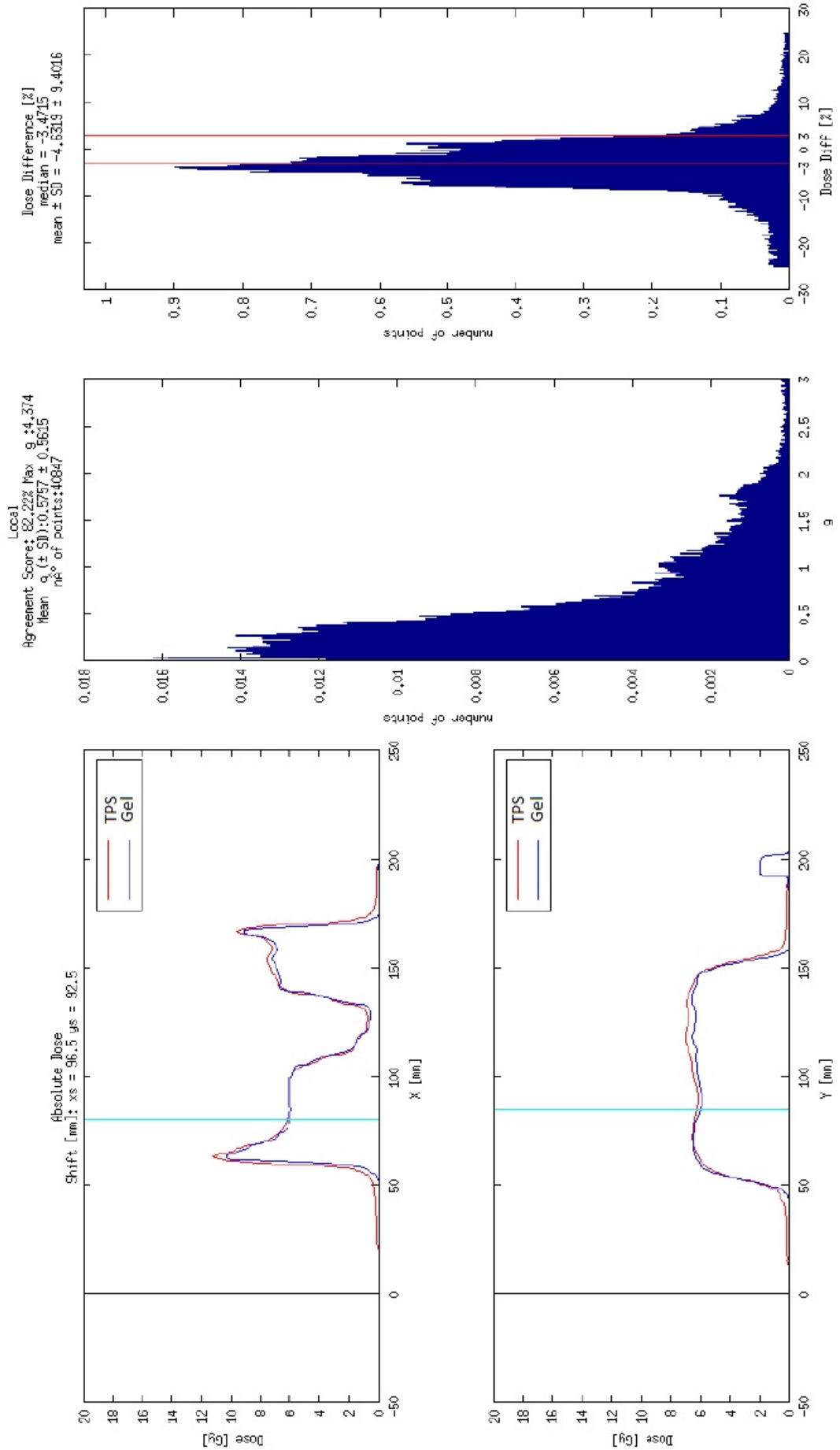

Figure 5: Dose profiles from cuboid A in the second run, slice 7.

Bibliography

[1] D. A. Low, W. B. Harms, S. Mutic, and J. A. Purdy, "A technique for the quantitative evaluation of dose distributions," *Medical physics*, vol. 25, no. 5, pp. 656–661, 1998.

[2] A. Cesario and F. Marcus, *Cancer systems biology, bioinformatics and medicine*. Springer, 2011.

[3] K. Harrington, "The biology of cancer," *Medicine*, vol. 44, pp. 1–5, 2016.

[4] L. Murray and M. Robinson, "Radiotherapy: technical aspects," *Medicine*, vol. 39, no. 12, pp. 689–704, 2011.

[5] R. A. Canters, I. M. Lips, M. Wendling, M. Kusters, M. Van Zeeland, R. M. Gerritsen, P. Poortmans, and C. G. Verhoef, "Clinical implementation of 3D printing in the construction of patient specific bolus for electron beam radiotherapy for non-melanoma skin cancer," *Radiotherapy and Oncology*, vol. xxx, no. 1, pp. 148–153, 2016.

[6] B. Mijnheer, S. Beddar, J. Izewska, and C. Reft, "In vivo dosimetry in external beam radiotherapy," *Medical physics*, vol. 40, no. 7, 2013.

[7] M. Silveira, J. Pavoni, and O. Baffa, "Three-dimensional quality assurance of imrt prostate plans using gel dosimetry," *Physica Medica*, vol. 34, pp. 1–6, 2017.

[8] J. Vandecasteele, *Optimisation and validation of three-dimensional polymer gel dosimetry and radiochromic gel dosimetry for clinical applications*. PhD thesis, Ghent University, 2013.

[9] M. Williams and A. McKenzie, "Can we afford not to implement in vivo dosimetry?," *The British journal of radiology*, 2014.

[10] L. A. DeWerd and M. Kissick, "The phantoms of medical and health physics," *The Phantoms of Medical and Health Physics: Devices for Research and Development, Biological and Medical Physics, Biomedical Engineering. ISBN 978-1-4614-8303-8. Springer Science+ Business Media New York, 2014*, vol. 1, 2014.

[11] J. Vandecasteele and Y. De Deene, "On the validity of 3d polymer gel dosimetry: I. reproducibility study," *Physics in medicine and biology*, vol. 58, no. 1, p. 19, 2012.

[12] J. Vandecasteele and Y. De Deene, "Evaluation of radiochromic gel dosimetry and polymer gel dosimetry in a clinical dose verification," *Physics in medicine and biology*, vol. 58, no. 18, p. 6241, 2013.

[13] W. Parker and H. Patrocinio, "Clinical treatment planning in external photon beam radiotherapy," *Radiation oncology physics: A handbook for teachers and students. Vienna: IAEA*, p. 219, 2005.

[14] M. Beyzadeoglu, G. Ozyigit, and C. Ebruli, "Clinical radiation oncology," in *Basic Radiation Oncology*, pp. 145–173, Springer, 2010.

[15] W. H. Organization *et al.*, "Quality assurance in radiotherapy," 1988.

[16] D. S. Chang, F. D. Lasley, I. J. Das, M. S. Mendonca, J. R. Dynlacht, *et al.*, *Basic radiotherapy physics and biology*. Springer, 2014.

[17] Y. Nishimura, R. Komaki, *et al.*, "Intensity-modulated radiation therapy," *Gan to kagaku ryoho. Cancer & chemotherapy*, vol. 41, no. 13, pp. 2539–2542, 2014.

[18] S. Yajnik, *Proton Beam Therapy: How Protons are Revolutionizing Cancer Treatment*. Springer Science & Business Media, 2012.

[19] M. Alber, S. Broggi, C. De Wagter, I. Eichwurzel, P. Engström, C. Fiorino, D. Georg, G. Hartmann, T. Knöös, A. Leal, *et al.*, "Guidelines for the verification of imrt," *ESTRO booklet*, vol. 7, 2008.

[20] C. De Wagter, "The ideal dosimeter for intensity modulated radiation therapy (imrt): What is required?," in *Journal of Physics: Conference Series*, vol. 3, p. 4, IOP Publishing, 2004.

[21] H. Bouchard and J. Seuntjens, "Ionization chamber-based reference dosimetry of intensity modulated radiation beams," *Medical physics*, vol. 31, no. 9, pp. 2454–2465, 2004.

[22] R. Prescribing and R. I.-M. P.-B. Therapy, "Icru report 83," *Supplement to ICRU Report*, vol. 50, 2010.

[23] E. B. Podgoršak, *Radiation physics for medical physicists*. Springer, 2006.

[24] J. Sorriaux, A. Kacperek, S. Rossomme, J. A. Lee, D. Bertrand, S. Vynckier, and E. Sterpin, "Evaluation of gafchromic® ebt3 films characteristics in therapy photon, electron and proton beams," *Physica Medica*, vol. 29, no. 6, pp. 599–606, 2013.

[25] R. Pecharromán-Gallego, A. Mans, J.-J. Sonke, J. C. Stroom, Í. Olaciregui-Ruiz, M. Herk, and B. J. Mijnheer, "Simplifying epid dosimetry for imrt treatment verification," *Medical physics*, vol. 38, no. 2, pp. 983–992, 2011.

[26] D. Palma, E. Vollans, K. James, S. Nakano, V. Moiseenko, R. Shaffer, M. McKenzie, J. Morris, and K. Otto, "Volumetric modulated arc therapy for delivery of prostate radiotherapy: comparison with intensity-modulated radiotherapy and three-dimensional conformal radiotherapy," *International Journal of Radiation Oncology* Biology* Physics*, vol. 72, no. 4, pp. 996–1001, 2008.

[27] A. K. Rath and N. Sahoo, *Particle Radiotherapy*. Springer, 2015.

[28] H. Paganetti, "Advancing (proton) radiation therapy," *International Journal of Radiation Oncology Biology Physics*, vol. 87, no. 5, pp. 871–873, 2013.

[29] J. L. Leman, "In vivo dosimetry; essential or unnecessary?," *Journal of Radiotherapy in Practice*, vol. 11, no. 01, pp. 55–61, 2012.

[30] S. Marcié, E. Charpiot, R.-J. Bensadoun, G. Ciais, J. Hérault, A. Costa, and J.-P. Gérard, "In vivo measurements with mosfet detectors in oropharynx and nasopharynx intensity-modulated radiation therapy," *International Journal of Radiation Oncology* Biology* Physics*, vol. 61, no. 5, pp. 1603–1606, 2005.

[31] P. E. Engström, P. Haraldsson, T. Landberg, H. Sand Hansen, S. Aage Engelholm, and H. Nyström, "In vivo dose verification of imrt treated head and neck cancer patients," *Acta Oncologica*, vol. 44, no. 6, pp. 572–578, 2005.

[32] F. Gagliardi, K. Roxby, P. Engström, and J. Crosbie, "Intra-cavitary dosimetry for imrt head and neck treatment using thermoluminescent dosimeters in a naso-oesophageal tube," *Physics in medicine and biology*, vol. 54, no. 12, p. 3649, 2009.

[33] R. Varadhan, J. Miller, B. Garrity, and M. Weber, "In vivo prostate imrt dosimetry with mosfet detectors using brass build-up caps.," *Journal of Applied Clinical Medical Physics*, vol. 7, no. 4, 2006.

[34] A. Vinall, A. Williams, V. Currie, A. Van Esch, and D. Huyskens, "Practical guidelines for routine intensity-modulated radiotherapy verification: pre-treatment verification with portal dosimetry and treatment verification with in vivo dosimetry," *The British journal of radiology*, 2014.

[35] M. van Zijtveld, M. Dirkx, M. Breuers, H. de Boer, and B. Heijmen, "Portal dose image prediction for in vivo treatment verification completely based on epid measurements," *Medical physics*, vol. 36, no. 3, pp. 946–952, 2009.

[36] S. M. Nijsten, B. J. Mijnheer, A. L. Dekker, P. Lambin, and A. W. Minken, "Routine individualised patient dosimetry using electronic portal imaging devices," *Radiotherapy and oncology*, vol. 83, no. 1, pp. 65–75, 2007.

[37] G. S. Ibbott, D. S. Followill, H. A. Molineu, J. R. Lowenstein, P. E. Alvarez, and J. E. Roll, "Challenges in credentialing institutions and participants in advanced technology multi-institutional clinical trials," *International Journal of Radiation Oncology* Biology* Physics*, vol. 71, no. 1, pp. S71–S75, 2008.

[38] I. P. Gerothanassis, A. Troganis, V. Exarchou, and K. Barbarossou, "Nuclear magnetic resonance (nmr) spectroscopy: basic principles and phenomena, and their applications to chemistry, biology and medicine," *Chemistry Education Research and Practice*, vol. 3, no. 2, pp. 229–252, 2002.

[39] A. Jirasek, C. Duzenli, C. Audet, and J. Eldridge, "Characterization of monomer/crosslinker consumption and polymer formation observed in ft-raman spectra of irradiated polyacrylamide gels," *Physics in medicine and biology*, vol. 46, no. 1, p. 151, 2001.

[40] J. Vandecasteele and Y. De Deene, "On the validity of 3d polymer gel dosimetry: Iii. mri-related error sources," *Physics in medicine and biology*, vol. 58, no. 1, p. 63, 2012.

[41] Y. De Deene, G. Pittomvils, and S. Visalatchi, "The influence of cooling rate on the accuracy of normoxic polymer gel dosimeters," *Physics in medicine and biology*, vol. 52, no. 10, p. 2719, 2007.

[42] J. Vandecasteele and Y. De Deene, "On the validity of 3d polymer gel dosimetry: Ii. physico-chemical effects," *Physics in medicine and biology*, vol. 58, no. 1, p. 43, 2012.

[43] Y. De Deene, P. Hanselaer, C. De Wagter, E. Achten, and W. De Neve, "An investigation of the chemical stability of a monomer/polymer gel dosimeter," *Physics in medicine and biology*, vol. 45, no. 4, p. 859, 2000.

[44] Y. De Deene, A. Venning, C. Hurley, B. Healy, and C. Baldock, "Dose–response stability and integrity of the dose distribution of various polymer gel dosimeters," *Physics in medicine and biology*, vol. 47, no. 14, p. 2459, 2002.

[45] K. Vergote, Y. De Deene, E. V. Bussche, and C. De Wagter, "On the relation between the spatial dose integrity and the temporal instability of polymer gel dosimeters," *Physics in medicine and biology*, vol. 49, no. 19, p. 4507, 2004.

[46] S. Michiels, A. D. Hollander, N. Lammens, M. Kersemans, G. Zhang, K. Poels, E. Sterpin, S. Nuyts, K. Haustermans, T. Depuydt, and J.-m. Denis, "Towards 3D printed multifunctional immobilization for proton therapy : Initial materials characterization Towards 3D printed multifunctional immobilization for proton therapy : Initial materials characterization," vol. 5392, 2016.

[47] F. M. Khan, "Physics of Radiation Therapy Third Edition," p. 1138, 2003.

[48] M. J. Butson, T. Cheung, P. Yu, and P. Metcalfe, "Effects on skin dose from unwanted air gaps under bolus in photon beam radiotherapy," *Radiation Measurements*, vol. 32, no. 3, pp. 201–204, 2000.

[49] M. Sroka, J. Reguła, and W. Łobodziec, "The influence of the bolus-surface distance on the dose distribution in the build-up region," *Reports of Practical Oncology and Radiotherapy*, vol. 15, no. 6, pp. 161–164, 2010.

[50] F. Chang, P. Chang, K. Benson, and F. Share, "Study of elasto-gel pads used as surface bolus material in high energy photon and electron therapy," *International Journal of Radiation Oncology, Biology, Physics*, vol. 22, no. 1, pp. 191–193, 1992.

[51] E. . Z. BEBIG, "Superflab: bolus material for external beam radiation therapy.," 2017. original document from Harris Semiconductor.

[52] F. printers, *FELIXbuilder 3D print software.* FELIX printers, 2017.

[53] Y. De Deene, K. Vergote, C. Claeys, and C. De Wagter, "The fundamental radiation properties of normoxic polymer gel dosimeters: a comparison between a methacrylic acid based gel and acrylamide based gels," *Physics in medicine and biology*, vol. 51, no. 3, p. 653, 2006.

[54] Y. De Deene, R. Van de Walle, E. Achten, and C. De Wagter, "Mathematical analysis and experimental investigation of noise in quantitative magnetic resonance imaging applied in polymer gel dosimetry," *Signal Processing*, vol. 70, no. 2, pp. 85–101, 1998.

[55] W. Crijns, F. Maes, U. Van Der Heide, and F. Van den Heuvel, "Calibrating page sized gafchromic ebt3 films," *Medical physics*, vol. 40, no. 1, 2013.

[56] M. Soret, S. L. Bacharach, and I. Buvat, "Partial-volume effect in pet tumor imaging," *Journal of Nuclear Medicine*, vol. 48, no. 6, pp. 932–945, 2007.

[57] P. Santago and H. D. Gage, "Statistical models of partial volume effect," *IEEE Transactions on Image Processing*, vol. 4, no. 11, pp. 1531–1540, 1995.

[58] Sun nuclear corporation, *1D SCANNER Reference Guide*, 2016.

[59] A. Karlsson, H. Gustavsson, S. Månsson, K. McAuley, and S. Å. J. Bäck, "Dose integration characteristics in normoxic polymer gel dosimetry investigated using sequential beam irradiation," *Physics in medicine and biology*, vol. 52, no. 15, p. 4697, 2007.

[60] P. Mann, M. Witte, T. Moser, C. Lang, A. Runz, W. Johnen, M. Berger, J. Biederer, and C. Karger, "3d dosimetric validation of motion compensation concepts in radiotherapy using an anthropomorphic dynamic lung phantom," *Physics in Medicine and Biology*, vol. 62, no. 2, p. 573, 2016.

Auteursrechtelijke overeenkomst

Ik/wij verlenen het wereldwijde auteursrecht voor de ingediende eindverhandeling:
Feasibility of a 3D printed bolus integrated with polymer gel dosimetry

Richting: **master in de industriële wetenschappen: nucleaire technologie-nucleaire technieken / medisch nucleaire technieken**
Jaar: **2017**

in alle mogelijke mediaformaten, - bestaande en in de toekomst te ontwikkelen - , aan de Universiteit Hasselt.

Niet tegenstaand deze toekenning van het auteursrecht aan de Universiteit Hasselt behoud ik als auteur het recht om de eindverhandeling, - in zijn geheel of gedeeltelijk -, vrij te reproduceren, (her)publiceren of distribueren zonder de toelating te moeten verkrijgen van de Universiteit Hasselt.

Ik bevestig dat de eindverhandeling mijn origineel werk is, en dat ik het recht heb om de rechten te verlenen die in deze overeenkomst worden beschreven. Ik verklaar tevens dat de eindverhandeling, naar mijn weten, het auteursrecht van anderen niet overtreedt.

Ik verklaar tevens dat ik voor het materiaal in de eindverhandeling dat beschermd wordt door het auteursrecht, de nodige toelatingen heb verkregen zodat ik deze ook aan de Universiteit Hasselt kan overdragen en dat dit duidelijk in de tekst en inhoud van de eindverhandeling werd genotificeerd.

Universiteit Hasselt zal mij als auteur(s) van de eindverhandeling identificeren en zal geen wijzigingen aanbrengen aan de eindverhandeling, uitgezonderd deze toegelaten door deze overeenkomst.

Voor akkoord,

Sevenois, Matthijs

Datum: **6/06/2017**